JCB Journal of Cell Biology

ARTICLE

VPS13A and VPS13C are lipid transport proteins differentially localized at ER contact sites

Nikit Kumar[1*], Marianna Leonzino[1,2,3,4,5*], William Hancock-Cerutti[1,2,3,4,5**], Florian A. Horenkamp[1**], PeiQi Li[1], Joshua A. Lees[1], Heather Wheeler[1,2,3,4,5], Karin M. Reinisch[1], and Pietro De Camilli[1,2,3,4,5]

Mutations in the human VPS13 genes are responsible for neurodevelopmental and neurodegenerative disorders including chorea acanthocytosis (VPS13A) and Parkinson's disease (VPS13C). The mechanisms of these diseases are unknown. Genetic studies in yeast hinted that Vps13 may have a role in lipid exchange between organelles. In this study, we show that the N-terminal portion of VPS13 is tubular, with a hydrophobic cavity that can solubilize and transport glycerolipids between membranes. We also show that human VPS13A and VPS13C bind to the ER, tethering it to mitochondria (VPS13A), to late endosome/lysosomes (VPS13C), and to lipid droplets (both VPS13A and VPS13C). These findings identify VPS13 as a lipid transporter between the ER and other organelles, implicating defects in membrane lipid homeostasis in neurological disorders resulting from their mutations. Sequence and secondary structure similarity between the N-terminal portions of Vps13 and other proteins such as the autophagy protein ATG2 suggest lipid transport roles for these proteins as well.

Introduction

A major path for the transport of bilayer lipids between membranes is vesicular transport. However, this route can be bypassed by lipid transport proteins that extract lipids from a membrane, shield them from the aqueous cytosolic environment within hydrophobic cavities, and deliver them to a target membrane. Often, these proteins also function as tethers between two participating organelles, thus making transport more efficient (Holthuis and Menon, 2014; Lahiri et al., 2015; Gatta and Levine, 2017; Saheki and De Camilli, 2017). Protein-mediated transport is particularly important for lipid exchange between the ER and mitochondria as these two organelles are not connected by membrane traffic, yet mitochondria use precursors imported from the ER to produce most of their lipids (Dimmer and Rapaport, 2017). Conversely, lipids generated in mitochondria can be delivered to the ER for distribution to other membranes (Voelker, 1984).

Yeast studies have suggested that the ER–mitochondria encounter structures (ERMES) complex mediates this bidirectional lipid transport between the ER and mitochondria (Kornmann et al., 2009; AhYoung et al., 2015; Jeong et al., 2016). However, other pathways for ER–mitochondria lipid transfer must also exist (Elbaz-Alon et al., 2014; Hönscher et al., 2014) as ERMES deletion is not lethal (Lang et al., 2015). A protein that may function in such a pathway is Vps13, as spontaneous gain-of-function mutations in its gene could rescue the growth defect of yeast ERMES mutants (Lang et al., 2015). Additionally, mutants lacking both ERMES and Vps13 are not viable (Lang et al., 2015). Vps13 localizes at contacts between the mitochondria and the vacuole (so called v-CLAMPs, for vacuole and mitochondria patches) and between the vacuole and the ER (nuclear–vacuole junction; NVJ; Lang et al., 2015). An interesting hypothesis is that Vps13 may mediate lipid transfer between the vacuole and other membranes and that it may provide an alternative indirect path for the flow of specific lipids between the ER and mitochondria via the vacuole. Defects in mitochondria membrane integrity observed in yeast mutants lacking either ERMES complex components or Vps13 (Hanekamp et al., 2002; Park et al., 2016) are consistent with this possibility. However, so far, there is no direct evidence that Vps13 can transfer lipids.

While the ERMES complex is not conserved in metazoan cells, members of the VPS13 family are expressed in all animal species, including humans, whose genome contains four VPS13 genes (VPS13A/Chorein, VPS13B, VPS13C, and VPS13D; Velayos-Baeza et al., 2004). The precise function of these proteins remains unclear, although they have been implicated in a variety of processes including membrane traffic at Golgi–endosome interfaces (De et al., 2017), cytoskeletal organization (Föller et al., 2012; Alesutan et

[1]Department of Cell Biology, Yale University School of Medicine, New Haven, CT; [2]Department of Neuroscience, Yale University School of Medicine, New Haven, CT; [3]Howard Hughes Medical Institute, Yale University School of Medicine, New Haven, CT; [4]Program in Cellular Neuroscience, Neurodegeneration and Repair, Yale University School of Medicine, New Haven, CT; [5]Kavli Institute for Neuroscience, Yale University School of Medicine, New Haven, CT.

*N. Kumar and M. Leonzino contributed equally to this paper; **W. Hancock-Cerutti and F.A. Horenkamp contributed equally to this paper; Correspondence to Pietro De Camilli: pietro.decamilli@yale.edu; Karin M. Reinisch: karin.reinisch@yale.edu.

al., 2013; Schmidt et al., 2013; Shiokawa et al., 2013; Honisch et al., 2015), calcium signaling (Pelzl et al., 2017), mitochondrial health (Lesage et al., 2016), and autophagy (Muñoz-Braceras et al., 2015; Lupo et al., 2016). Interestingly, stretches of primary sequence similarity have been noted between VPS13 and ATG2, another protein of unknown function that is required for phagophore formation (Wang et al., 2001; Velikkakath et al., 2012). More specifically, similarities occur in the first ∼120 residues at the N terminus (referred to as the Chorein_N domain) and in a stretch of ∼70 aa in the C-terminal region (termed ATG_C in Pfam; Pfisterer et al., 2014; Muñoz-Braceras et al., 2015; Tamura et al., 2017).

Human VPS13 proteins are of great biomedical interest as loss-of-function mutations in each of them are associated with genetic diseases: chorea acanthocytosis, a Huntington-like syndrome associated with red cell shape abnormalities (VPS13A; Rampoldi et al., 2001; Ueno et al., 2001); Cohen syndrome, a complex multisystem condition characterized by global developmental delay and intellectual disability (VPS13B; Kolehmainen et al., 2003); an early onset form of Parkinson's disease (VPS13C; Lesage et al., 2016); and a recently described form of ataxia with spasticity (VPS13D; Gauthier et al., 2018; Seong et al., 2018). Determining the function of these proteins will be key in elucidating the mechanisms of these diseases.

In this study, we demonstrate that the N-terminal region of Vps13 is a lipid transport module that can harbor glycerolipids and transfer them between bilayers. We also show that VPS13A, the closest homologue of yeast Vps13, localizes at contacts between the ER and mitochondria, suggesting that VPS13A may fulfill some of the functions of the ERMES complex in mammalian cells. Surprisingly, VPS13C, the paralogue most closely related to VPS13A, is instead localized at contacts between the ER and late endosomes/lysosomes, revealing that duplication of VPS13 during evolution correlates with diversification of their sites of action.

Results

VPS13A and VPS13C are localized at organelle contact sites

To gain first insights into the properties of VPS13A, the chorea acanthocytosis gene, we investigated its subcellular localization. As available antibodies did not detect the protein by immunofluorescence (IF), we tagged it at a site found to preserve yeast Vps13 function (Park et al., 2016; VPS13A^Halo or ^mCherry) and expressed it in Cos-7 or HeLa cells. By far the majority of the VPS13A signal occurred in the form of small patches arranged to form elongated structures (Fig. 1 A, left). Coexpression of a mitochondrial marker (mito-BFP) and an ER marker (EGFP-Sec61β) identified these structures as mitochondrial profiles lying in close proximity to the ER (Fig. 1, A and B; line scans in Fig. 1 C; Fig. S1 A; and quantification in Fig. S1 B). Furthermore, in these cells, i.e., where VPS13A was overexpressed, areas of close proximity between the ER and mitochondria were increased (Fig. S1 C). These findings are consistent with an ER-to-mitochondria tethering function of VPS13A, consistent with the possibility that in metazoa, VPS13A may fulfill some of the functions of ERMES.

In some cells, VPS13A fluorescence signal also appeared in the form of small doughnut-shaped spots that overlapped with the ER marker (Sec61β; Fig. 1 D, inset a) but not with mitochondria (Fig. S1 D). These structures were negative for preinternalized dextran (an endocytic tracer; Fig. S1 E) and for markers of the endolysosomal system (Fig. S1 F) and were instead identified as lipid droplets based on labeling with the neutral lipid marker BODIPY 493/503 (Fig. 1 E). Correlative fluorescence EM analysis of VPS13A-transfected cells confirmed that VPS13A fluorescent doughnuts were lipid droplets enwrapped by ER tubules (Fig. 1 F). EM also showed that contacts between the ER and lipid droplets were more abundant in VPS13A-overexpressing cells than in WT cells (Fig. S1 G).

Lack of localization of VPS13A on organelles of the endolysosomal system was surprising as it contrasted with the localization of yeast Vps13 at contact sites between the vacuole and other membranes (Lang et al., 2015). We thus asked whether VPS13C, a Parkinson's disease–linked protein and the closest paralogue to VPS13A among human VPS13 proteins, was also absent from these organelles. VPS13C is similar to VPS13A throughout its length, with the exception of the presence of an ∼500-aa insert after position 807 most likely corresponding with a duplication of the upstream region. When VPS13C^mClover3 (tagged at the cognate site used for VPS13A) was coexpressed with VPS13A^mCherry in HeLa or Cos-7 cells, striking differences were observed in the localization of the two proteins (Figs. 2 A and S2 A). No localization of VPS13C at mitochondria was observed (Fig. S2 A). A major pool of VPS13C was instead localized on vesicular and tubular structures negative for VPS13A (Figs. 2 A and S2 A) but positive for preinternalized dextran and generally surrounded by ER (Fig. 2 B), suggesting that VPS13C populates contacts between ER and the endolysosomal system. Some of these vesicles were positive for the lysosomal marker LAMP1 (Fig. S2 B) or for Rab7 (Fig. 2 C), consistent with the reported binding of VPS13C to this Rab (McCray et al., 2010). A smaller pool of VPS13C did colocalize with VPS13A on doughnut-like structures (Fig. 2 A, arrowheads, and Fig. S2 A, arrowheads) that surrounded LipidTOX-stained lipid droplets (Fig. 2 D), in agreement with the previously reported association of VPS13C with lipid droplets based on subcellular fractionation (Yang et al., 2016) and IF (Ramseyer et al., 2018). Lack of VPS13C at mitochondria contacts was unexpected as its mutations have been linked to mitochondrial dysfunction and Parkinson's disease (Lesage et al., 2016). However, mitochondrial dysfunction could represent an indirect effect of abnormalities in intracellular lipid transport.

Expression of tagged protein yields optimal fluorescence signal but may produce artifacts of overexpression. Thus, the localization of VPS13A and VPS13C was further validated by immunostaining HeLa cells in which the corresponding genes were edited to encode proteins with 2×HA epitopes at the same sites used to tag the exogenous proteins (Fig. S2 C). The analysis of these cells, where VPS13A and VPS13C are expressed at endogenous levels, confirmed the differential localization of the two proteins at sites of contacts between the ER and mitochondria and between the ER and endolysosomes, respectively (Fig. 2, E–H; and Fig. S2 D). One difference was that in all cases, only spot-like contacts between the ER and these other organelles were detected, indicating that the more extensive localization of VPS13A and VPS13C at organelle interfaces are due to expansions of these contacts as a result of overexpression.

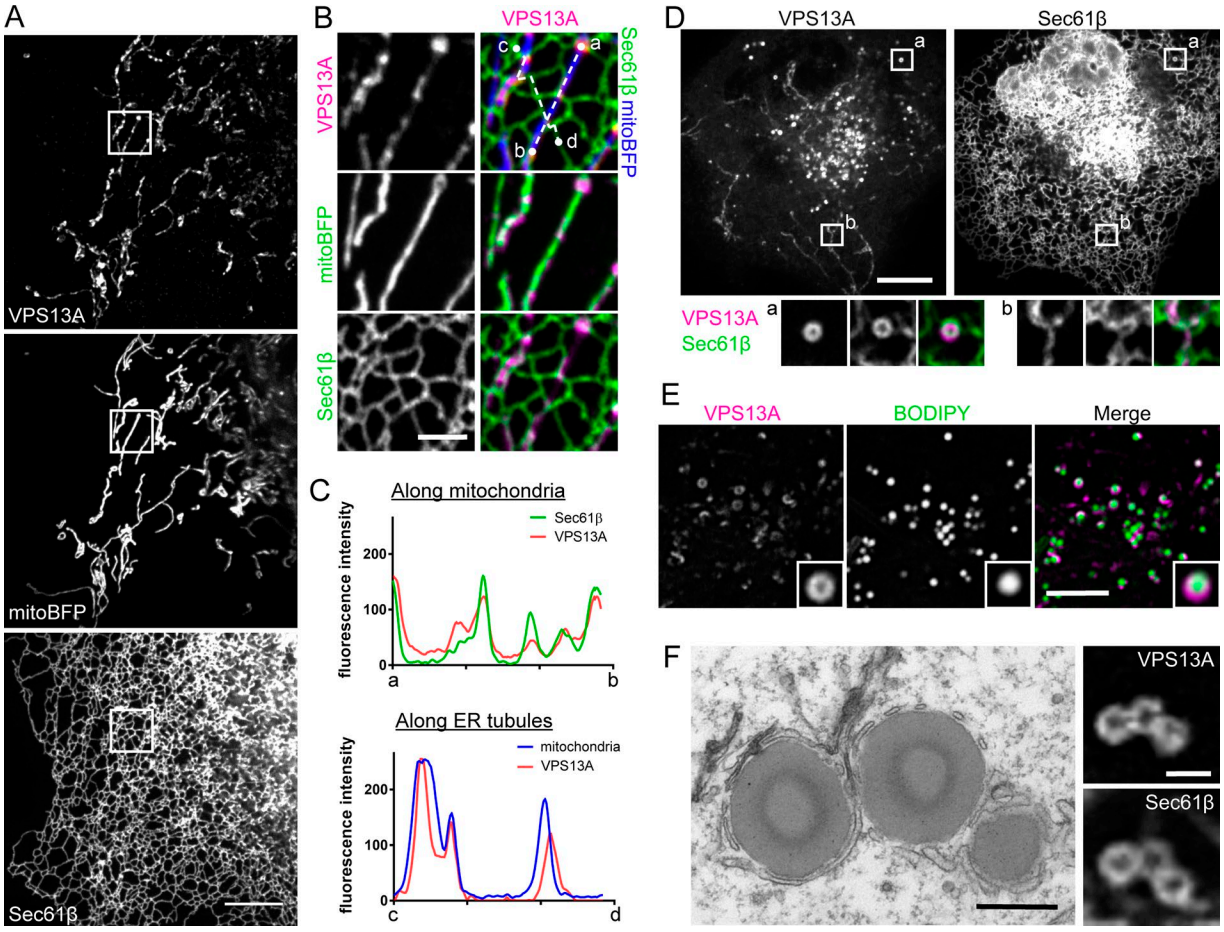

Figure 1. **VPS13A localizes at ER–mitochondria and ER–lipid droplet contact sites. (A)** Cos-7 cell expressing VPS13A^Halo, GFP-Sec61β, and mito-BFP showing overlap of VPS13A fluorescence with both mitochondria and ER. Bar, 10 µm. **(B)** High magnifications of the region indicated by white squares in A showing precise localization of VPS13A at sites of contact between ER and mitochondria. Bar, 2 µm. **(C)** Fluorescence intensity for the three indicated channels along a line either tracing the long axis of a mitochondrion (top) or ER tubules (bottom). Lines used for the plots are indicated by dashed lines in the merged image in B. **(D)** A Cos-7 cell expressing VPS13A^Halo and GFP-Sec61β shows two patterns of VPS13A fluorescence both overlapping with the ER: dots (doughnuts; a) and elongated structures (b), shown at high magnification in the bottom panels. Bar, 10 µm; bottom panels, 3 × 3 µm. **(E)** Live staining of neutral lipids with BODIPY 493/503 in a Cos-7 cell expressing VPS13A^Halo showing the presence of VPS13A around lipid droplets (insets). Bar, 5 µm; insets, 1.5 × 1.5 µm. **(F)** Correlative light EM of a Cos-7 cell expressing VPS13A^mChweey and GFP-Sec61β. Fluorescent images of three lipid droplets (right) and corresponding cell region shown by EM (left) demonstrate abundant presence of ER around the lipid droplets. Bars: 0.5 µm (left); 1 µm (right).

FFAT motifs in VPS13A and VPS13C mediate tethering of the ER

A function of VPS13A and VPS13C in bridging the ER to other organelles requires the presence of binding sites responsible for these localizations. Bioinformatics analysis of VPS13 revealed a domain organization conserved from yeast to humans. A long N-terminal region of unknown fold (VPS13α) was followed by putative WD40 modules, a domain reminiscent of a DH domain (DH-Like domain; DH_L) and a previously predicted C-terminal pleckstrin homology (PH) domain (Fig. 3 A; Fidler et al., 2016). An FFAT motif, a short amino acid sequence known to interact with the ER VAMP-associated protein (VAP), is present in the Vps13α region of both proteins as previously noted (Murphy and Levine, 2016). Accordingly, full-length VPS13A harboring the FFAT mutation ($VPS13A^{FFLI}$) was no longer tethered to the ER but rather was localized to the entire outer surface of mitochondria and of lipid droplets (Fig. S2 E). The same localization was observed for WT VPS13A when expressed in VAP-knockout (KO) cells (Fig. S2 F; Dong et al., 2016). Likewise, N-terminal constructs (VPS13α) of both proteins ($VPS13A_{1–1,372}$ and $VPS13C_{1–1,390}$) accumulated over the entire ER, more so upon cotransfection with VAP (VAPB; Figs. 3 B and S2 G), while the same constructs harboring mutations of the FFAT motif ($VPS13A_{1–1,372}^{FFLI}$ and $VPS13C_{1–1,390}^{YFSL}$) had a diffuse cytosolic distribution (Fig. 3 C). Furthermore, overexpression of VAPB together with VPS13C induced the formation of abnormal ER structures, completely enwrapping all VPS13C-positive endosomes (Fig. 3 D). These findings not only confirm the role of the FFAT motif in anchoring these proteins to the ER but also indicate that binding sites for mitochondria (in VPS13A), late endosomes/lysosomes (in VPS13C), and lipid droplets (both proteins) are localized in the C-terminal regions of the two proteins.

C-terminal regions of VPS13A and VPS13C contain binding sites for other organelles

A fragment of VPS13A comprising its entire WD40 region had a cytosolic distribution (Fig. 4 A), while a corresponding fragment of VPS13C ($VPS13C_{2,415–3,309}$) fragment decorated the

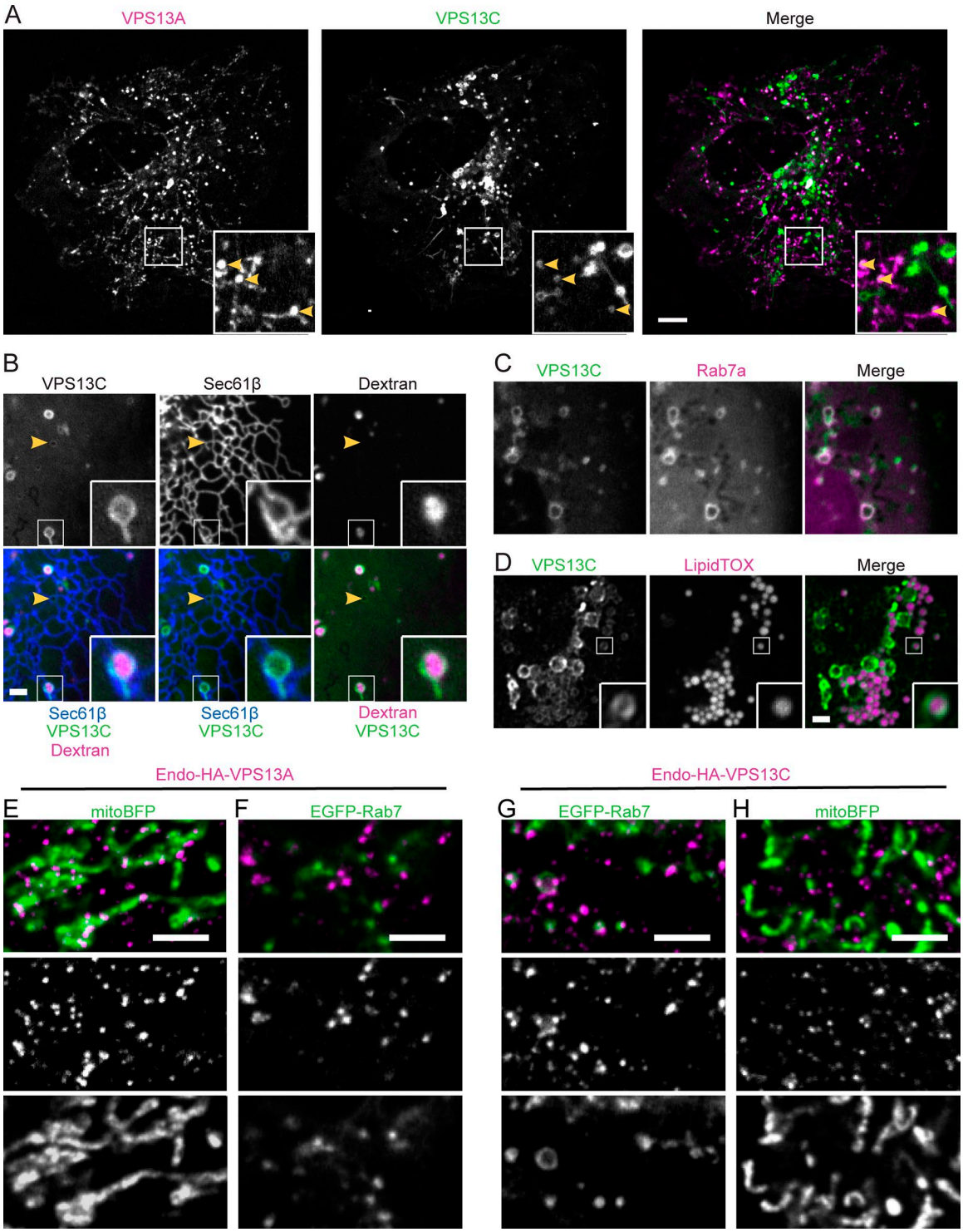

Figure 2. **VPS13C localizes at ER–endosome contacts. (A)** HeLa cells expressing VPS13A^mCherry and VPS13C^mClover3 show minimal overlap between the VPS13A and VPS13C signals specifically found on small round structures likely to be lipid droplets (arrowheads in insets). Bar, 10 µm; insets, 10 × 10 µm. **(B)** Cos-7 cells expressing VPS13C^mClover3 or RFP-Sec61β and loaded overnight with dextran Alexa Fluor 647 show VPS13C signal surrounding dextran-positive puncta, which are often surrounded by ER. Arrowheads point to a dextran-negative vesicle enwrapped by ER, likely to be a lipid droplet. Insets, 2.73 × 2.73 µm. **(C)** The majority of full-length VPS13C^mClover3 localizes on Rab7a-RFP–positive structures in Cos7 cells. **(D)** Cos-7 cells expressing VPS13C^mClover3 loaded overnight with 100 µM oleate and then fixed and stained with LipidTox. The figure shows VPS13C signal surrounding LipidTox-labeled spots (lipid droplets at high magnification in the inset) and more intense VPS13C signal around larger vesicular structures likely to be endolysosomal vesicles. Insets, 2.4 × 2.4 µm. **(E–H)** CRISPR/Cas9-edited HeLa cells expressing VPS13A or VPS13C tagged with 2×HA epitopes (endo-HA-VPS13A and endo-HA-VPS13C) at their genomic loci. Cells were transfected with either mito-BFP or EGFP-Rab7a, fixed, and immunostained with anti-HA antibodies (magenta). A large fraction of endo-HA-VPS13A–immunoreactive puncta are localized on mitochondria (E) and not on Rab7-positive vesicles (F). Conversely, a large fraction of endo-HA-VPS13C–immunoreactive puncta are localized on Rab7-positive vesicles (G) and not on mitochondria (H). Bars, 2 µM (B–H).

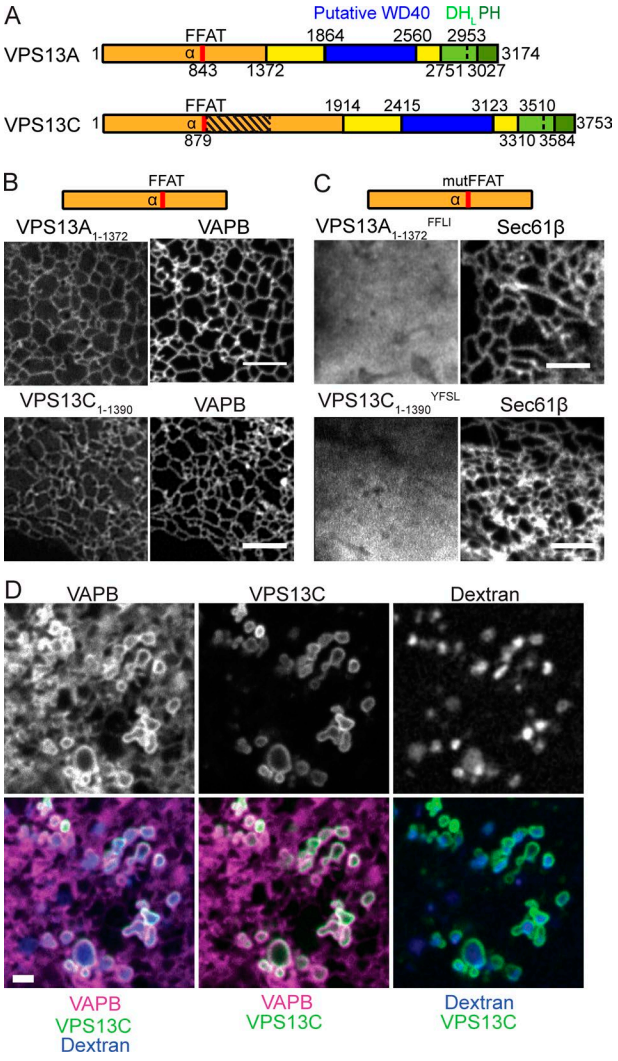

Figure 3. **The predicted FFAT motif in VPS13A and VPS13C tethers them to the ER. (A)** Schematic cartoon of the putative domain architecture of human VPS13A and VPS13C. The striped region in VPS13C represent an ∼500-residue insertion likely arisen from the internal duplication of the region just upstream of it. The dashed line in the DH_L domain defines the start of the ATG homology region (see also Fig. 5 A). **(B)** Cos-7 cells expressing $VPS13A_{1–1,372}$-EGFP or $VPS13C_{1–1,390}$-EGFP and mCherry-VAPB show robust enrichment of VPS13A and VPS13C N-terminal fragments on the ER. **(C)** Corresponding constructs bearing a mutant FFAT motif ($VPS13A_{1–1,372}^{FFLI}$ and $VPS13C_{1–1,390}^{YFSL}$) expressed in Cos-7 cells are instead cytosolic. Bar, 5 µm. **(D)** In VAPB-overexpressing cells, VPS13C populates VAP-enriched ER domains that completely surround endocytic vesicles filled with dextran. Bar, 2 µm. All amino acid numbers refer to human proteins.

entire surface of vesicles positive for dextran (Fig. S3 A), Rab7 (Fig. 4 B), or LAMP1 (Fig. S3 B), thus identifying the WD40 module as the binding site for late endosomes/lysosomes in VPS13C. Further analysis of the localization of deletion constructs of VPS13A and VPS13C identified the DH_L-PH domains as (i) the mitochondria-binding region of VPS13A and (ii) the lipid droplet–binding region of both proteins (Fig. 4, C and D). The DH_L-PH domain sequence contains a region of high similarity to ATG2, which also binds lipid droplets (Velikkakath et al., 2012; Tamura et al., 2017). Accordingly, this region alone, fused to EGFP, labeled lipid droplets (Fig. 4 E). Within this region, an amino acid stretch almost identical in VPS13A (aa 2,993–3,027) and VPS13C (aa 3,550–3,584) is predicted to fold as an amphipathic helix, a structural motif used by some proteins to interact with lipid droplets (Rowe et al., 2016). Mutation of one residue (conserved between VPS13A and VPS13C) on the hydrophobic face of such helix completely abolished its lipid droplet localization (Fig. 4 F). An additional amphipathic helix was previously predicted within the same region of VPS13A (aa 2,959–2,982; Drin et al., 2007) but not in VPS13C and may justify the stronger recruitment on lipid droplets observed for VPS13A with respect to VPS13C.

A more precise identification of the mitochondria-binding region of VPS13A was achieved by generating chimeric constructs containing subdomains of the DH_L-PH region from VPS13A and VPS13C (Fig. S3 C). This demonstrated that both the ATG homology region and the PH domain of VPS13A are sufficient to drive mitochondrial localization (Fig. S3, D–G), suggesting a bipartite binding site. This site resides downstream of the region shown to mediate binding to mitochondria in yeast Vps13. However, as the yeast mitochondrial Vps13 interactor MCP1 (John Peter et al., 2017) is not conserved in mammals, a nonconserved mode of binding to mitochondria appears likely.

The N-terminal portion of VPS13 has lipid transport properties

The localization of at least two VPS13 isoforms at organelle contact sites is consistent with a potential conserved role of VPS13 family proteins in lipid transport between adjacent organelles. Thus, we next tested directly the possibility that Vps13 might bind and transport lipids. Vps13 is a large protein (molecular weight > 340 kD), and so far, we could not produce full-length proteins from either humans or other organisms in sufficient quantities for biochemical analysis. Thus, we used VPS13 fragments. As the predicted WD-40, DH_L, and PH domains are unlikely lipid transport modules, we focused on the N-terminal region Vps13α (Fig. 5 A), whose structure and function were unknown. Not only is Vps13α well conserved within the VPS13 family across species, but the most N-terminal region (Chorein_N domain) shows homology with other proteins including ATG2 (De et al., 2017).

We were successful in purifying Vps13α from *Saccharomyces cerevisiae* (residues 1–1,350) and showed by negative-stain EM that it forms monomeric or dimeric rods, although the dimeric forms may not occur for the full-length protein (Fig. S4, A and B). Potential lipid content of this fragment, expressed in Expi293F cells and affinity purified, was assessed by liquid chromatography–tandem mass spectrometry (LC/MS/MS). Vps13α bound to glycerophospholipids but not other lipid species, with enrichment of PC relative to the glycerolipid content of cellular membranes (Fig. 5 B). Despite rigorous washes of the protein before lipid analysis, there were ∼10 glycerolipids associated per protein molecule. This indicates that Vps13α might bind multiple lipid molecules at once, consistent with studies described below. Further supporting that the protein harbors phospholipids, Vps13α comigrated with the fluorescently labeled lipids NBD-PS and NBD-PA and to a lesser extent with NBD-phosphatidylethanloamine (PE) and NBD-ceramide on a native gel (Fig. 5 C).

We used these observations in designing a FRET-based in vitro assay to interrogate whether Vps13α can transfer lipids between membranes. We mixed donor liposomes containing DGS-NTA,

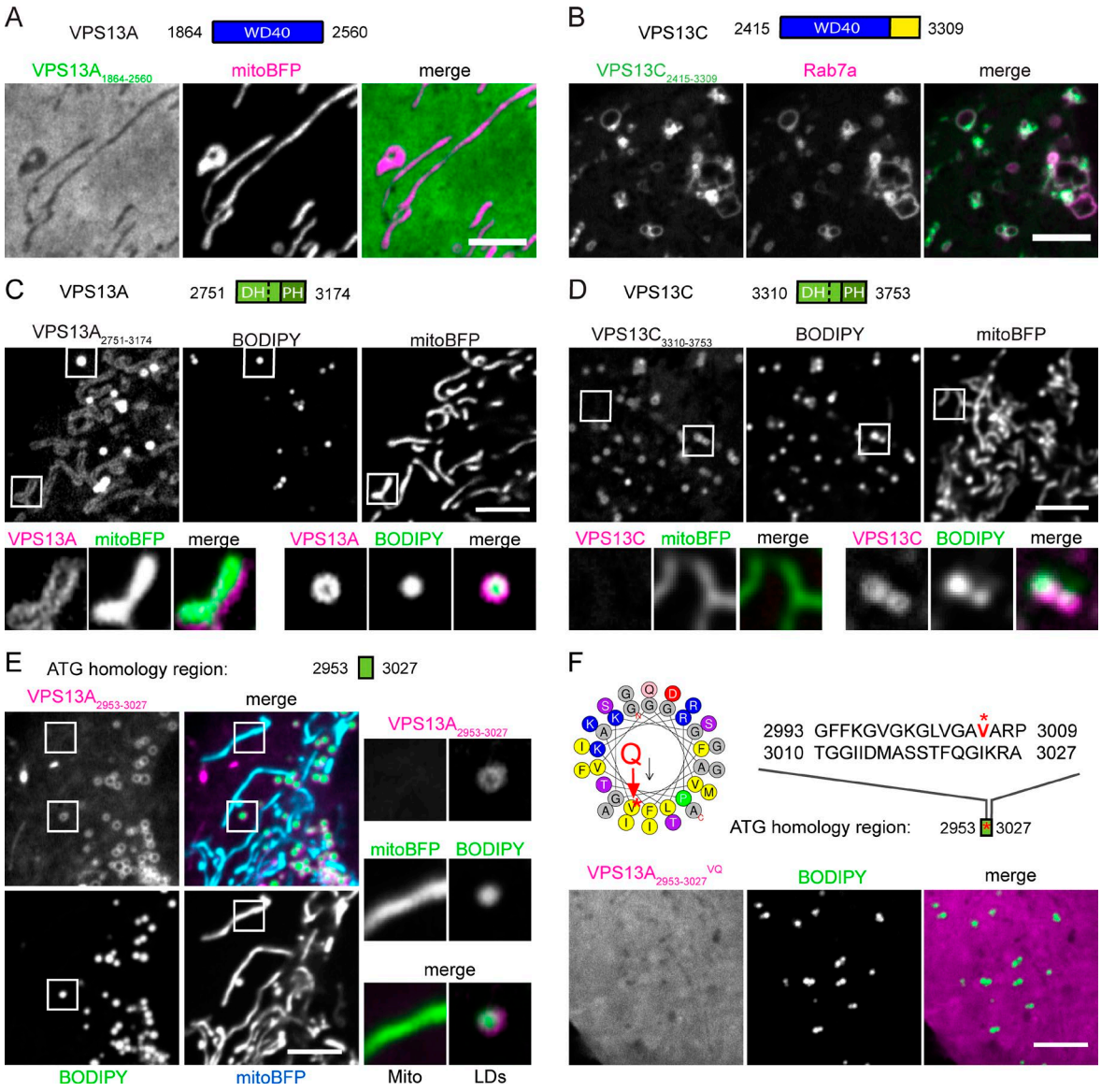

Figure 4. **Binding regions for mitochondria or late endosomes lie in the C-terminal half of VPS13 proteins. (A)** Cos-7 cells expressing mClover3-VPS13C$_{2,415–3,309}$ and Rab7a-mCherry show localization of VPS13C signal on Rab7a-positive vesicles. **(B)** EGFP-tagged VPS13A$_{1,864–2,560}$ has a cytosolic localization with no accumulation at the surface of mitochondria, which appear dark in the EGFP channel due to the exclusion of cytosol. **(C)** Cos-7 cells coexpressing mCherry-tagged VPS13A$_{2,751–3,174}$ and mito-BFP were incubated with BODIPY 493/503 for lipid droplet (LD) labeling. VPS13A$_{2,751–3,174}$ fluorescence clearly outlines mitochondria and lipid droplets as shown in high-magnification panels below (2.33 × 2.33 µm). **(D)** Cos-7 cells expressing mClover3-VPS13C$_{3,310–3,753}$ and labeled with BODIPY 493/503 show VPS13C$_{3,310–3,753}$ signal surrounding BODIPY-positive puncta (lipid droplets) but not mitochondria as shown in high-magnification panels below (2.33 × 2.33 µm). **(E)** Cos-7 cells coexpressing the mitochondrial marker mito-BFP and an mCherry-tagged VPS13A fragment (VPS13A$_{2,953–3,027}$) corresponding with the ATG homology region show that this fragment surrounds lipid droplets (labeled with BODIPY 493/503) but not mitochondria. Regions indicated by the white squares are shown in high magnification on the right (2.33 × 2.33 µm). **(F)** Representation of the predicted helical arrangement of residues 2,993–3,010 of VPS13A generated via the HeliQuest tool (heliquest.ipmc.cnrs.fr; Gautier et al., 2008). An mCherry-tagged VPS13A$_{2,953–3,027}$ construct bearing a single amino acid substitution (V3006Q; indicated by an asterisk) in the hydrophobic face of the predicted amphipathic helix had a cytosolic localization. All micrographs were acquired by live-cell imaging, and images shown are representative of at least two independent experiments. Bars, 5 µm. All amino acid numbers refer to human proteins.

NBD-PS, and rhodamine-PE with acceptor liposomes containing PI(4,5)P_2 and lacking fluorescent labeling, and then we added Vps13α$_{tethered}$. In this chimeric construct, the Vps13α fragment is tethered to the liposomes via a C-terminal hexahistidine sequence that interacts with DGS-NTA on the donor liposomes and an upstream N-terminal PH module that interacts with PI(4,5)P_2 on the acceptor liposomes (Figs. 5 D and S5, A and B). Initially, FRET between NBD and rhodamine in the donor liposomes quenched NBD fluorescence. If either NBD-PS or rhodamine-PE or both were transported to acceptor liposomes, the fluorophores were diluted, and the distance separating them increased, leading to decreased FRET and an increase in NBD fluorescence (Figs. 5 D and S5 A; Struck et al., 1981; Saheki et al., 2016; Yu et al., 2016).

In the transfer assay, NBD fluorescence increased after addition of Vps13α$_{tethered}$, consistent with a role for Vps13α in lipid transfer. Fluorescence increase was not due to fusion or

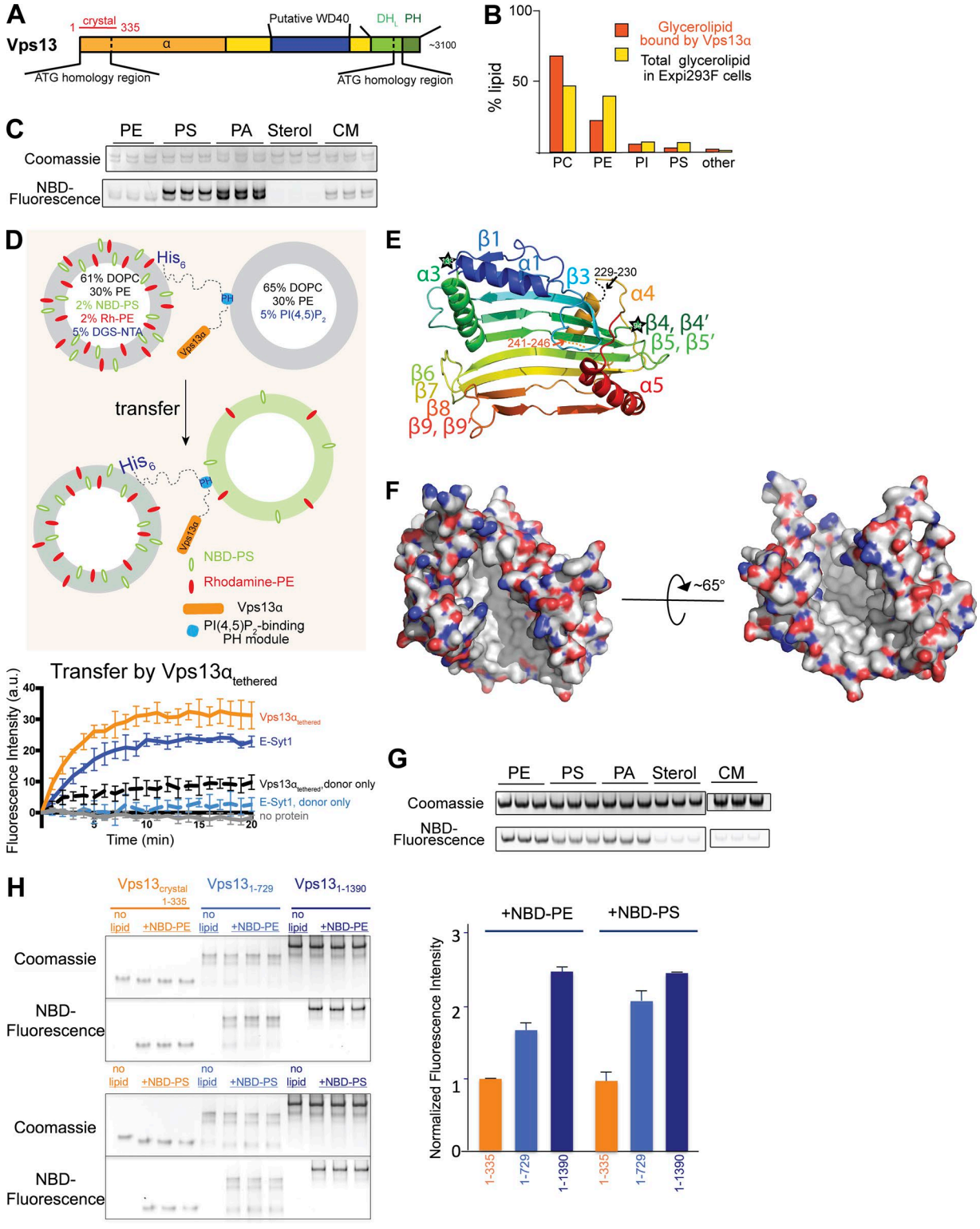

Figure 5. **N-terminal portions of Vps13 solubilize and transport lipids. (A)** Schematic of VPS13 domain architecture. The crystallized fragment from *C. thermophilum* is indicated. **(B)** LC/MS/MS analysis of lipids that copurify with Vps13α showed binding to glycerolipids, with a slight preference for PC. Cellular abundance of these glycerolipids is indicated (Lees et al., 2017). Sphingomyelin represented 1% of bound lipids. No sterol, di-, or triacylglycerides were detected. **(C)** Vps13α was incubated with NBD-tagged lipid including NBD-ceramide (CM) and then examined by native PAGE. Phospholipids, which were visualized by their fluorescence, comigrated with protein, visualized by Coomassie staining. **(D)** Donor liposomes (25 µM) containing fluorescent lipids (2% NBD-PS, 2% NBD-PE, 5% DGS-NTA, 61% DOPC, and 30% PE) were mixed 1:1 with acceptor liposomes (25 µM: 65% DOPC, 30% PE, and 5% $PI(4,5)P_2$) in the presence or absence of $Vps13α_{tethered}$ (0.125 µM). This construct tethers the Vps13α fragment between acceptor and donor liposomes via a $PI(4,5)P_2$-specific PH domain and a C-terminal hexahistidine sequence. The assay monitors the increase in NBD-PS fluorescence after lipid transfer from donor liposomes, where NBD fluorescence is quenched via FRET with Rhodamine-PE, to acceptor liposomes. The fluorescence increase observed is consistent with lipid transfer at a rate similar to that for

hemifusion between donor and acceptor liposomes as the increase in turbidity of the liposome mixture after addition of Vps13α$_{tethered}$ (due to the clustering of liposomes induced by this construct) was rapidly reversed by the addition of a protease (Fig. S5). The fluorescence increase was due to lipid transfer by Vps13 and not to extraction from donor liposomes only, as in the absence of acceptor liposomes, i.e., in an extraction-only scenario, the assay resulted in a much smaller increase of fluorescence (Fig. 5 D). Similar results were obtained by replacing Vps13α in the tethering construct with the lipid transport module of Extended-Synaptotagmin (Schauder et al., 2014; Yu et al., 2016), which served as a positive control (Fig. 5 D). Thus, in vitro transfer assays showed that Vps13α can transfer glycerolipids between membranes in vitro. Since both the Extended-Synaptotagmins and Vps13α bind and thus likely also transport glycerolipids like PC and PE (Schauder et al., 2014; see also LC/MS/MS analysis above), the major constituents of liposomes in the assay, overall lipid transfer by these proteins may be much faster than that observed for fluorescent lipids only.

The N-terminal region of VPS13 contains a hydrophobic cavity

Sequence similarity between the N-terminal regions of VPS13 and the autophagy protein ATG2 (Pfisterer et al., 2014; De et al., 2017) hinted that these proteins might share a common module at their N termini and guided construct design for structural studies. After crystallization trials with VPS13 N-terminal fragments from various species, we succeeded in crystallizing a fragment comprising residues 1–335 (Vps13$_{crystal}$) from the fungus *Chaetomium thermophilum*, and we solved its structure to a resolution of 3.0 Å using the single-wavelength anomalous dispersion method (Hendrickson, 1991). A poorly conserved, predicted loop (residues 228–236) was truncated to facilitate crystallization. Data collection and refinement statistics are in Table 1.

Vps13$_{crystal}$ folds to resemble a utility scoop lacking the handle, and based on DALI searches of the Protein Database, it bears no significant structural similarity to any previously characterized protein (Figs. 5 E and S5 C). N-terminal α-helices (α1 and α3) help to cap one end of the scoop, whereas loops and the most C-terminal α-helix (α5) define its edges. β-strand elements form the scoop base, whose convex backside is buttressed by helix α4. A long predicted helical segment (α2), which connects strand β4′ to helix α3 (residues marked by stars in Fig. 5 E) and thus must extend over and partially cover the concave face of the scoop, was not ordered in the crystal and was not modeled. While the convex backside of Vps13$_{crystal}$ is covered by hydrophilic residues, the concave face is lined exclusively by hydrophobic residues (Fig. 5 F) and is therefore well suited for solubilizing hydrophobic fatty acyl chains of phospholipids. The hydrophobic cavity of Vps13$_{crystal}$, measuring ∼20 Å across, has approximately twice the diameter of the cavity of previously studied lipid transporters and so could accommodate several lipid molecules simultaneously.

Indeed, Vps13$_{crystal}$ retains some of the lipid-binding abilities of Vps13α (Fig. 5 G). Secondary structure predictions are consistent with the presence of at least two more Vps13$_{crystal}$-like modules in the N-terminal portions of Vps13. To compare the number of fluorescent lipids bound by Vps13$_{crystal}$ versus longer constructs twice or four times its size (Vps13$_{1–729}$ comprising residues 1–729 or Vps13$_{1–1,390}$ comprising residues 1–1,390 of C. *thermophilum* Vps13), we used gel-shift experiments as described above. We found that Vps13$_{1–729}$ and Vps13$_{1–1,390}$ bind approximately twice and 2.5 times as many fluorescent lipids as Vps13$_{crystal}$ (Fig. 5 H). Thus, we propose that Vps13$_{crystal}$ is part of a larger lipid-binding unit in the intact protein. Full-length Vps13 could harbor several Vps13$_{crystal}$-like modules, or alternatively, Vps13$_{crystal}$ could be part of an elongated tube reminiscent of lipid transporters like ERMES or bacterial lipopolysaccharide transporter complexes (AhYoung et al., 2015; Sherman et al., 2018). Vps13$_{crystal}$ could form one end of a tubular structure running the length of the Vps13α rod since their diameters match (Fig. S4 B). The secondary structure predictions for Vps13 are consistent with either model (Fig. S6).

Taken together with the lipid harboring data and transfer assays, the finding that Vps13α and Vps13$_{crystal}$ harbor a lipid-binding module or modules supports a lipid-transfer function for Vps13. Based on homology with ATG2, our findings raise the possibility that the N-terminal region of ATG2 may also transfer lipids. Preservation of lipid transfer function does not require high sequence conservation beyond that the residues in the cavity be hydrophobic and those outside hydrophilic (Fig. S4 C).

Discussion

Collectively, our findings point to VPS13 proteins as lipid transporters at organelle contact sites (Fig. 6). They further indicate that as the single *Vps13* gene underwent duplications during evolution, specific functions have segregated in different paralogues. The robust localization of VPS13A at ER–mitochondria contacts is of special interest given the partially overlapping function of Vps13 and ERMES in yeast (Lang et al., 2015; Park et al., 2016). As a complex homologous to ERMES does not appear to be present

the lipid transport domain of Extended-Synaptotagmin1 (0.125 µM), a previously validated glycerolipid transporter (Saheki et al., 2016; Yu et al., 2016; Bian et al., 2018). The Extended-Synaptotagmin1 lipid-transfer domain was tethered between liposomes analagously to Vps13α via a hexahistidine tag and a PH domain. The fluorescence increase is much smaller when only donor but not acceptor liposomes are present. The small but still significant fluorescence increase under these conditions is due to lipid extraction by Vps13α$_{tethered}$ and would not be expected in the case of Vps13α-mediated fusion of hemifusion between donor liposomes. The dithionate and turbidity assays (Fig. S5, A and B) rule out Vps13α-mediated fusion and/or hemifusion between liposomes. The experiments were performed in triplicate. SD is indicated. **(E)** Ribbons diagram for Vps13$_{crystal}$ colored from blue (N terminus) to red (C terminus). Predicted helix α2 (not depicted) connects residue 94 to residue 133 (stars). **(F)** Surface representation with carbon atoms shown in white, oxygens in red, and nitrogens in blue. View as in E (left) and rotated (right). The concave face of the scoop is entirely hydrophobic. **(G)** Vps13$_{crystal}$ comigrates with NBD-labeled glycerolipids. **(H)** Vps13$_{crystal}$, Vps13$_{1–729}$, and Vps13$_{1–1,390}$ were quantitated against BSA standards using SDS-PAGE. Equimolar quantities of these proteins were incubated with fluorescent glycerolipids (NBD-PS and NBD-PE) and then run on a native gel. Vps13$_{1–729}$ and Vps13$_{1–1,390}$, which are about twice and four times as large as Vps13$_{crystal}$, bound approximately twice and 2.5× as many fluorescent lipids/protein molecule, respectively. Each experiment was performed in triplicate. SD is indicated.

Table 1. **Crystallographic statistics**

Data collection	
Space group	$P2_1$
Unit cell dimensions (a, b, c in Å; α, β, γ in °)	58.93, 85.98, 71.03, 90, 93.67, and 90
Wavelength (Å)	0.9791
Resolution (Å)	48.59-3.0 (3.18-3.0)
R_{merge}	0.10 (0.334)
I/σ	21.9 (8.4)
Completeness (%)	99.9 (99.9)
Redundancy	20.4 (19.2)
Refinement	
Resolution (Å)	48.6-3.0
No. of unique reflections	14,328
R_{free}/R_{work} (%)	26.23/23.49
No. of non-hydrogen atoms (protein)	4,007
Average B (Å^2)	102
Root mean square deviation	
Bond length (Å)	0.011
Bond angle (°)	1.456
Ramachandran plot	
Favored (% residues)	98.4
Allowed (% residues)	1.6
Disallowed (% residues)	0

Numbers in parenthesis refer to values in the highest resolution bin.

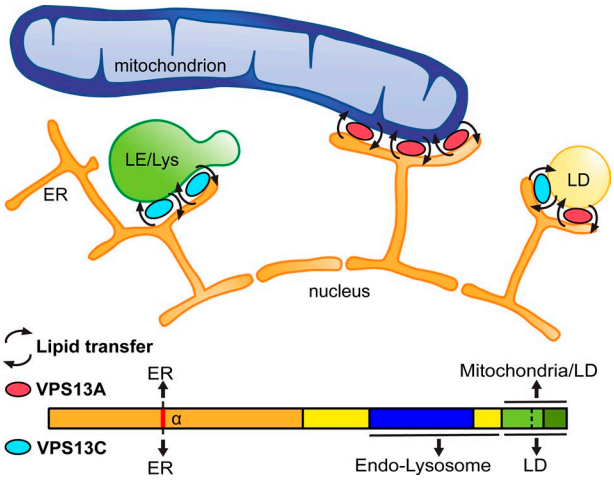

Figure 6. **Diagram depicting sites of action of VPS13A and VPS13C.** Schematic of VPS13A and VPS13C localization and domains responsible for such localization. LD, lipid droplet; LE, late endosome; Lys, lysosome.

in metazoans, VPS13A may have taken over its role. As loss of VPS13A function results in a neurodegenerative conditions but not in embryonic lethality, VPS13A likely cooperates with other proteins in lipid transport (Galmes et al., 2016; Hirabayashi et al., 2017). These may include VPS13B (whose C-terminal region we have found in preliminary experiments to bind mitochondria) or VPS13D, whose loss results in mitochondrial abnormalities (Anding et al., 2018; Seong et al., 2018). The localization of VPS13C at contacts of the ER with the endolysosomal system was somewhat unexpected since the study first reporting a causative link between VPS13 mutations and Parkinson's disease also reported a partial association of endogenous VPS13C with mitochondrial membranes and a role of VPS13 in mitochondrial function (Lesage et al., 2016). These findings were in line with strong evidence linking mitochondria defects to Parkinson's disease (Hang et al., 2015). However, mitochondrial dysfunction could be an indirect consequence of defects of the endolysosomal system, and several recent studies have linked genetic forms of Parkinson's disease to endolysosomal proteins (reviewed in Abeliovich and Gitler, 2016). Moreover, the clear association of VPS13C with late endosomes/lysosomes shown in this study is consistent with the many reported functional connections between VPS13 family members and the endolysosomal system in unicellular organisms (Samaranayake et al., 2011; Lang et al., 2015; Muñoz-Braceras et al., 2015), *Drosophila melanogaster* (Vonk et al., 2017), and mammalian cells (Seifert et al., 2011, 2015). The association with lipid droplets, which was previously reported in yeast lacking an ER–lipid droplet tethering complex (Grippa et al., 2015), raises the possibility that VPS13 may help transfer lipids not only between membranes but also between these lipid stores and specific cellular membranes. It remains possible that the localizations reported in this study may be subject to regulation depending upon the functional state of the cells as yeast Vps13 localizes at different organelle interfaces depending upon growth conditions (v-CLAMP versus NVJ; Lang et al., 2015).

The atomic structure of $Vps13_{crystal}$ and our in vitro lipid transport data indicate that the N-terminal portion of Vps13 forms a lipid transport domain. While these data were obtained with Vps13 from fungi, bioinformatic analysis predicts that the structure of Vps13α is conserved through evolution, suggesting preservation of function (Fig. S6). The $Vps13_{crystal}$ fragment has no structural similarity to any characterized lipid-transfer module beyond the general feature of a hydrophobic cavity that shields lipids from the aqueous environment during their transport through the cytosol. The ability of Vps13α to solubilize multiple lipids at once is atypical (Wong et al., 2017), though it is shared by some lipid transporters in the tubular lipid–binding protein (TULIP) family like ERMES (Jeong et al., 2016) or the Extended-Synaptotagmins (Schauder et al., 2014). The Chorein_N domain has been noted in several other proteins (Pfisterer et al., 2014; De et al., 2017) including ATG2, and its presence likely indicates that they have lipid transport modules similar to Vps13. Indeed, VPS13 and ATG2 may be founding members of a protein family with bulk lipid transport properties.

Bulk lipid transfer by VPS13 family members, in addition to controlling the lipid homeostasis of different membranes, could provide a source of lipids for membrane generation and/or expansion. For example, yeast Vps13, which associates with the spindle pole body component Cdc31 (De et al., 2017), is required for the growth of the prospore membrane that nucleates around this site (Park and Neiman, 2012; Park et al., 2013). Interestingly,

lipid droplets were shown to form direct contacts with this membrane (Hsu et al., 2017). ATG2, which has structural similarities to VPS13 both in its N-terminal and C-terminal (ATG_C) region (Pfisterer et al., 2014) and which also binds lipid droplets (Velikkakath et al., 2012), is required for an unrelated but similar process (Knorr et al., 2012): the maturation/closure of the autophagosome membrane (Velikkakath et al., 2012; Pfisterer et al., 2014). The most attractive scenario is that ATG2's still unknown mechanism of action in this process may involve transfer of lipids from other membranes and, in cells that contain them, from lipid droplets.

A key implication of our study is that defects in lipid dynamics likely play an important role in the clinical manifestations of patients with mutations in VPS13 isoforms, which include major movement disorders such as chorea acanthocytosis (VPS13A) and Parkinson's disease (VPS13C). They also suggest that different properties of each isoform, rather than (or in addition to) their different pattern of cell and tissue expression, may explain the different manifestations of disrupting mutations in VPS13 isoform. An enigmatic feature of the disease resulting from VPS13A mutations (chorea and acanthocytosis, i.e., neurodegeneration and misshaped erythrocytes) is the abnormal shape of red cells (Bird et al., 1978), but it is intriguing that other similar conditions are caused by mutations in proteins involved in lipid metabolism (Walsh et al., 2016; Aoun et al., 2017) or organelle tethering (Holmes et al., 2001). Addressing the precise function of each isoform with loss-of-function studies in cells and intact organisms will be a priority of future investigations. It is expected that these studies may help shed new insight into pathological mechanisms of neurodegenerative conditions.

Materials and methods

Reagents

Halo tag ligands JF549 and JF647 were a kind gift from L. Lavis (Janelia Farm, Ashburn, VA). Human VPS13A (transcript variant 1A) and VPS13C (transcript variant 2A) ORFs were purchased from Origene. The following constructs were kind gifts: mito-BFP and mCherry-Rab7a from G. Voeltz (University of Colorado Boulder, Boulder, CO; 49151 and 61804, respectively; Addgene), GFP-Rab5a from M. Zerial (Max Planck Institute of Molecular Cell Biology and Genetics, Dresden, Germany), EGFP-Rab7 from B. van Deurs (University of Copenhagen, Copenhagen, Denmark), EGFP-Lamp1 from S. Ferguson (Yale University, New Haven, CT), RFP-Lamp1 from W. Mothes (Yale University, New Haven, CT), and Sec61b-GFP and RFP from T. Rapoport (Harvard University, Cambridge, MA). mCherry-VAPB was previously generated in our laboratory (Dong et al., 2016). All the other ORFs used are listed in Table S1. Primary antibodies against HA (3F10; Roche), VPS13A (NBP1-85641; Novus Biological), VPS13C (HPA043507; Sigma-Aldrich Prestige), and GAPDH (40-1246; Proteus) were purchased commercially. Secondary antibodies (Alexa Fluor 594–conjugated goat anti-rat and Alexa Fluor 594–conjugated donkey anti-goat) were purchased from Thermo Fisher Scientific.

All EM reagents were purchased from Electron Microscopy Sciences. Lipids were purchased from Avanti Polar Lipids: DOPC (850357), NBD-PE (810144), NBD-PS (810198), NBD-PA (810138), NBD-ceramide (810211), Rhodamine-PE (810150), DGS-NTA (Ni; 790404), PI(4,5)P_2 (840046), liver PE (840026), and NBD-cholesterol (810252).

Bioinformatic analysis

Secondary structure prediction was performed through DisMeta software (Huang et al., 2014), and structure prediction was performed through RaptorX (Källberg et al., 2012) and Phyre2 (Kelley et al., 2015).

Generation of constructs

The coding sequences for Vps13 from *C. thermophilum* corresponding with residues 1–335 or 1–729 were cloned from genomic DNA into a modified pET-Duet vector containing a C-terminal 6×His tag. The coding sequence corresponding with residues 1–1,390 was cloned into a pCMV-6 vector containing an N-terminal 3×FLAG tag. The coding sequence for Vps13 from *S. cerevisiae* corresponding with residues 1–1,350, or Vps13α, was amplified from genomic DNA and cloned using the same strategy. For Vps13$\alpha_{tethered}$, the same sequence was fused the unstructured region of human E-Syt2 (649–739)–His_6, with the PH domain of rat PLCΔ (11–140) inserted after residue 689 using overlap extension PCR, and was cloned into a pCMV-6 vector containing an N-terminal 3×FLAG tag. E-Syt1 (93–327) containing the synaptotagmin, mitochondrial, and lipid-binding protein (SMP) lipid transport domain was fused to the PH domain of rat PLCΔ (11–140) and cloned into a pET-28a vector containing an N-terminal His_6 tag (Bian et al., 2018). Most constructs were generated with regular cloning protocols or through site-directed mutagenesis. Desired ORFs were amplified by PCR and inserted in vectors through enzymatic digestion and ligation. Unless otherwise stated, pmCherry and pEGFP (Takara Bio Inc.) were used as cloning vectors. Primer sets, enzymes, and vectors used for each construct are displayed in Table S1.

For internal tagging of VPS13A, the EGFP ORF was removed from the pEGFP vector through enzymatic digestion (XhoI/NotI), and the PCR-amplified VPS13A sequence was ligated. Restriction enzyme sites (SalI/ApaI) were introduced after aa 1,372 via site-directed mutagenesis, and mCherry or Halo tag ORFs flanked by short linkers (AGG/GG) were then inserted. Mito-GFP and mito-mCherry were generated from mito-BFP by swopping the fluorescent protein sequence using BamHI/NotI digestion. Internally tagged VPS13C and chimeric constructs were generated using InFusion cloning according to the manufacturer's protocol. All ORFs were fully sequenced after cloning.

Protein expression and purification

A fragment of Vps13 from *C. thermophilum* corresponding with residues 1–335 or 1–729 was expressed in BL21 (DE3) Codon Plus (Agilent) *Escherichia coli* cells. Cells were grown at 37°C to an OD_{600} of 0.6–0.8, when protein expression was induced with 0.5 mM IPTG, and then cells were cultured at 18°C for another 16–20 h. Selenomethionine-substituted protein was expressed as previously described (Doublié, 1997). Cells were pelleted, resuspended in buffer A (20 mM Hepes, pH 7.8, 300 mM NaCl, 20 mM imidazole, and 5% glycerol) containing 1× complete EDTA-free protease inhibitor cocktail (Roche) and lysed in an Emulsiflex-C5

cell disruptor (Avestin). Cell lysates were clarified via centrifugation at 27,000 *g* for 30 min. To collect the protein, supernatant was incubated with Ni-NTA resin (QIAGEN) for 1 h at 4°C, and then the resin was washed with 3× 10 bed volumes of buffer A. Retained protein was eluted from the resin with buffer A supplemented with 300 mM imidazole, concentrated in a 10-kD molecular weight cutoff (MWCO) Amicon centrifugal filtration device, and loaded onto a Superdex 75 16/60 column (GE Healthcare) equilibrated with buffer B (20 mM Hepes, pH 7.8, and 150 mM NaCl) or buffer C (20 mM Hepes, pH 7.8, 300 mM NaCl, 1 mM Tris(2-carboxyethyl)phosphine [TCEP], and 2.5% glycerol) for selenomethionine-substituted protein. Peak fractions containing pure Vps13 were recovered and concentrated.

$Vps13_{1–1,390}$ (from *C. thermophilum*), Vps13α, and $Vps13α_{tethered}$ (from *S. cerevisiae*) were each expressed in Expi293 cells (Invitrogen) according to the manufacturer's instructions for 72 h. Cells were pelleted, resuspended in buffer C, and lysed via sonication. Cell lysates were clarified via centrifugation at 27,000 *g* for 20 min, and the supernatant was incubated with preequilibrated anti-FLAG M2 affinity resin (Sigma-Aldrich) for 2 h. The resin was washed with 3× 10 bed volumes of buffer C and incubated for 16 h with buffer C containing 1 mM ATP and 2 mM $MgCl_2$. The protein was eluted with buffer C supplemented with 0.2 mg/ml 3× FLAG peptide and concentrated in a 30-kD MWCO Amicon centrifugal filtration device.

Protein crystallization, structure determination, and refinement

Crystals of selenomethionine-substituted *C. thermophilum* Vps13 (1–335 Δ228–236)–His_6 at 6 mg/ml were grown at 37°C using the sitting-drop vapor-diffusion method. Equal volumes of protein were mixed with mother liquor containing 100 mM Bis-Tris, pH 6.5–6.7, and 34–38% 15/4 pentaerythritol ethoxylate (Hampton). Drops were equilibrated against well solution containing 1 M NaCl. Crystals, which belonged to spacegroup $P2_1$ and had two copies of $Vps13_{crystal}$ in the asymmetric unit, were harvested in cryoloops and flash frozen. Diffraction data were collected at NE-CAT beamline 24-ID-C at the Advanced Photon Source and integrated, scaled, and merged using X-ray Detector Software and Aimless (Kabsch, 2010; Evans, 2011). Data from four crystals collected at the selenium edge were combined in the final dataset, and phases were calculated using the single-wavelength anomalous dispersion method (Hendrickson, 1991). We identified the selenium positions, calculated experimental phases and density-modified maps, and built an initial model using the phenix AutoSol pipeline (Adams et al., 2010). Because diffraction was anisotropic, completeness dropped abruptly at resolutions better than 3 Å, and maps calculated at higher resolutions showed no improvement. Accordingly, the final model was refined to a resolution of 3.0 Å by multiple cycles of manual model rebuilding in coot (Emsley et al., 2010) followed by positional, individual isotropic B-factor and Translation Libration Screw refinement with phenix.refine (Adams et al., 2010) using secondary structure restraints. We modeled residues 2–228, 231–240, and 247–317 (numbering refers to the loop-deleted sequence) in one of the $Vps13_{crystal}$ copies; some of these residues were disordered in the second copy (2–5, 19–22, 30–33, 221–226, and 240–247) and were omitted from the model. Figures were made using PyMOL (v1.8.6.0) software.

Lipid analysis of Vps13 by mass spectrometry

S. cerevisiae Vps13α (aa 1–1,350) was expressed and purified as described above with the following modifications. Following immunoprecipitation, FLAG resin–bound Vps13α was washed with 3× 20 bed volumes of buffer C for 30 min, after which it was incubated for 16 h with buffer containing 1 mM ATP and 2 mM $MgCl_2$. The protein was eluted with buffer supplemented with 0.2 mg/ml 3× FLAG peptide and concentrated in a 30-kD MWCO Amicon centrifugal filtration device to ∼0.5 mg/ml final concentration. The purified protein sample was sent to Avanti Polar Lipids for lipid analysis, where bound lipids were extracted in 2:1 (vol/vol) methanol:choroform. The chloroform layer was dried, and lipids were reconstituted with internal standards for phosphatidylcholine (PC), PE, phosphatidylinositol (PI), phosphatidylserine (PS), phosphatidic acid (PA), phosphatidylglycerol (PG), sphingomyelin (SM), triacylglycerol (TAG), DAG, and cholesterol-d7 for quantitation. The sample was injected into a reversed-phase C8 column with a gradient elution profile for the resolution of each lipid class and detected by an AB Sciex 5500 tandem mass spectrometer. The molecular species of lipids was quantified based on internal standards and summed by lipid class.

Liposome preparation

To prepare liposomes for lipid-transfer assays, lipids in chloroform were mixed in the indicated ratios and dried to thin films. Lipids were subsequently reconstituted in buffer containing 20 mM Hepes, pH 7.8, 300 mM NaCl, and 5% glycerol at a total lipid concentration of 1 mM and subjected to 10 freeze–thaw cycles alternating between liquid nitrogen and 37°C water bath. Crude liposomes were then extruded through a polycarbonate filter with 100 nm pore size a total of 21 times via a mini extruder (Avanti Polar Lipids) and used within 24 h.

In vitro lipid-binding assay

1 µl of either NBD-labeled PE, PS, PA, cholesterol, or ceramide (1 mg/ml in methanol) was incubated with 19 µl purified Vps13α or $Vps13_{crystal}$ (2 mg/ml) for either 30 min at 37°C or 2 h at 4°C. Samples were visualized on 10% native PAGE gels. NBD fluorescence was visualized using an ImageQuant LAS4000 (GE Healthcare), and total protein was visualized with Coomassie staining.

In vitro lipid-transfer FRET assays

Lipid-transfer reactions were performed in 50-µl volumes in 96-well plates (Nunc) containing a protein:lipid ratio of 1:400, with 0.125 µM protein, 25 µM donor liposomes (61% DOPC, 30% liver PE, 2% NBD-PS, 2% Rhodamine-PE, and 5% DGS-NTA [Ni]) and 25 µM acceptor liposomes (65% DOPC, 30% liver PE, and 5% $PI(4,5P)_2$). Fluorescence intensity of NBD was measured via excitation at 460 nm and detection at 538 nm every 1 min for 30 min at 30°C using a Synergy H1 Plate Reader (BioTek). All data were corrected by subtracting baseline from no-protein controls.

For the liposome fusion–control assay, we used the dithionite assay as previously described (Weber et al., 1998; Shi et al., 2013). Briefly, after performing a lipid-transfer reaction (as described

above), 2.5 µl freshly prepared dithionite buffer (100 mM dithionite [Sigma-Aldrich] in 50 mM Tris, pH 10) was added to reactions, and NBD fluorescence was monitored for an additional 20 min.

The turbidity assay, which rules out fusion and hemifusion, was performed as previously described (Bian et al., 2018). We used the same constructs and concentration of proteins and liposomes in the same volume as for the lipid-transfer assay. Following addition of the protein to the liposomes, absorbance at 405 nm was measured every 30 s for 10 min; then, cocktail (10 µl) containing 1.8 M imidazole and 1.15 mg/ml proteinase K (Sigma-Aldrich) was added, and absorbance was monitored for an additional 10 min. All data were corrected by subtracting background signal before protein addition.

Cell culture and transfection

HeLa and Cos-7 cells (obtained from ATCC) were maintained at 37°C in a humidified atmosphere at 5% of CO_2 in DMEM (Thermo Fisher Scientific) supplemented with 10% FBS (Thermo Fisher Scientific), 100 U/ml penicillin, 100 mg/ml streptomycin, and 2 mM GlutaMAX (Thermo Fisher Scientific). EXPI293 were grown in EXPI293 expression medium upon constant shaking. All cell lines were routinely tested and always resulted as free from mycoplasma contamination.

Generation of 2×HA-tagged VPS13A and VPS13C CRISPR–knock-in HeLa cell line

For the insertion of a 2×HA tag in the endogenous locus of either VPS13A or VPS13C in HeLa cells, asymmetric single-stranded DNA (ssDNA) donor repair templates designed as described by Richardson et al. (2016) were used. Cas9-mediated cut was directed by single-guide RNA obtained by mixing a fluorescent tracrRNA ATTO 550 (IDT) and a specific CRISPR RNA (crRNA; see Table S1). Ribonuclear complexes were obtained by incubating the two RNA components with the purified Cas9 (IDT) and the donor ssDNA (see Table S1) and then transfected into low-passage HeLa cells using Mirus TransIT-X2 transfection reagent. 24 h after transfection, cells containing the fluorescent tracrRNA were selected by FACS sorting, and single positive cells were seeded in 96-well plates. Single clones were allowed to grow and then were tested for HA expression by Western blotting. Positive clones were used for subsequent IF.

As expected for such large proteins (>360 kD), the endogenous levels of expression are so low that a conventional IF protocol with rat anti-HA primary antibody (MBL) followed by Alexa Fluor 594–conjugated goat anti-rat secondary antibody did not produce a signal strong enough to be detected by microscopy. To amplify the signal, an additional incubation with a tertiary Alexa Fluor 594–conjugated donkey anti-goat antibody was used. Moreover, to improve the signal-to-noise ratio, each of the antibodies used was subjected to a clearing procedure as follows: WT HeLa cells were fixed in 4% PFA, washed in 50 mM glycine in PBS, double-rinsed in PBS, and then scraped in PBS containing 1% BSA and 1% Triton X-100. Antibodies were added to the fixed cell lysate at a concentration 3.5× higher than the final concentration used for IF and were incubated by rotation on a wheel overnight at 4°C. Cell debris were then pelleted by spinning the tubes at 17,000 *g* for 20 min at 4°C, and the supernatant containing cleared antibodies was diluted 3.5× in PBS containing 1% BSA.

Fixed- and live-cell imaging

For microscopy, cells were seeded on glass-bottomed Mat-Tek dishes (Mat-Tek Corporation) 5,500/cm^2 in complete media without antibiotics and transfected 16 h later with FugeneHD (Promega). Spinning-disk confocal imaging was performed 20–24 h after transfection using a Nikon T*i*-E inverted microscope equipped with the Improvision UltraView VoX system (PerkinElmer) and controlled by Volocity (Improvision) software. Images were acquired with a Plan Apochromat objective (60× 1.45 NA). During imaging, cells were maintained in live-cell imaging buffer (Thermo Fisher Scientific) in a humidified atmosphere at 37°C.

Halo tag ligands JF549 and JF647 were used at a final concentration of 200 nM. Cells were incubated with the dye for 1 h, rinsed, and then incubated in complete media for 1 h before imaging. For dextran internalization, cells were incubated with 10 µg/ml dextran–Alexa Fluor 488 or dextran–Alexa Fluor 647 (3,000 molecular weight; Thermo Fisher Scientific) for 30 min or overnight in complete culture media. Live staining of lipid droplets with BODIPY 493/503 (Sigma-Aldrich) was performed in complete media (final concentration of 1 µM) for 20 min at 37°C followed by a 10-min wash in complete media right before imaging. For staining of lipid droplets with LipidTox reagent (Thermo Fisher Scientific) in fixed cells, cells were fixed in freshly prepared PFA (4% in phosphate buffer, pH 7.5) for 20 min at room temperature and then washed in PBS. PBS-diluted LipidTox reagent was added to cells following manufacturer's instructions.

Correlative fluorescence and EM microscopy

Cells were seeded on gridded glass-bottomed Mat-Tek dishes and transfected with VPS13A^mCherry and GFP-Sec61β as described above. Cells expressing VPS13A and showing doughnut-shaped structures positive for both VPS13A and the ER marker were identified with the spinning-disk microscope (see above for settings) and localized on the grid using the transmitted light channel. Cells were then fixed in 2.5% glutaraldehyde–0.1 M sodium cacodylate and post-fixed with 1% OsO_4 in 1.5% K4Fe(CN)$_6$ and 0.1 M sodium cacodylate, followed by en bloc staining with 2% uranyl acetate, dehydration in ethanol, and embedding in Embed 812. Using the grid as a guide, the selected cells were identified under a light microscope and then cut and contrasted with uranyl acetate and lead citrate. Samples were imaged with a Philips CM-10 transmission electron microscope. ER–lipid droplet contact sites (defined as region of <20 nm distance between membranes) were counted and measured in length using iTEM software (Olympus).

Image processing, analysis, and statistics

Florescence images presented are representative of cells imaged in at least three independent experiments and were processed with FIJI (ImageJ; National Institutes of Health) software. *Unsharp Mask* and *Gaussian blur* filters were applied on some of the images presented, and the dimension of higher-magnification insets were doubled using the *Scale* function of FIJI.

Quantifications were performed on unprocessed single-plane ROIs of 400 μm^2 obtained from at least three independent experiments. Area of overlap between VPS13A signal and ER or mitochondria were obtained by generating a mask of the thresholded signal from Sec61β or mito-BFP channels, respectively, and then adding this mask on the thresholded VPS13A channel. The percentage of VPS13A signal within the mask over the total thresholded VPS13A signal area was then calculated. ER–mitochondria contacts were quantified with an analogous approach, generating a mask of the thresholded mito-BFP channel and calculating the percentage of the thresholded Sec61β-positive area that overlaps with that mask. Quantification of the area of overlap between endogenous VPS13A-HA or VPS13C-HA signal with mitochondria or late endosomes was performed by making a mask of the thresholded signal from Mito-GFP or EGFP-Rab7 signal and adding this mask on the thresholded HA channel. The percentage of HA signal within the mask over the total thresholded HA signal area was then quantified on a per-cell basis. Comparisons between conditions were conducted using one-way ANOVA followed by Tukey's honest significant difference test using GraphPad Prism software.

For the evaluation of ER–lipid droplet contacts in EM images, three cells per condition from two independent experiments were analyzed. For each cell, a single section of the middle plane of the cell was used. Statistical analysis was performed with Prism. Groups were compared using a two-tailed Student's *t* test, and results were deemed significant when $P > 0.05$.

Online supplemental material

Fig. S1 shows how VPS13A localizes at ER–mitochondria and ER–lipid droplet contacts and not on endolysosomes. Fig. S2 shows VPS13A and VPS13C localizations. Fig. S3 shows regions of VPS13A and VPS13C that bind mitochondria and late endosomes/lysosomes. Fig. S4 shows low-resolution characterization of the VPS13 N-terminal region. Fig. S5 shows lipid transfer assays showing that Vps13α does not promote membrane fusion or hemifusion. Fig. S6 shows multiple sequence alignment for the VPS13 N terminus (Vps13α; CLUSTALOmega). Table S1 shows a list of constructs generated in this study.

Acknowledgments

We are grateful to Tim Levine (University College London, London, UK), Xin Bian, and Mirko Messa (our laboratories) for discussion and advice.

This work was supported by grants from the National Institutes of Health (NS36251, DA018343, and DK45735 to P. De Camilli, GM08616 to K.M. Reinisch, TG GM008283 to N. Kumar, and Medical Science Training Program TG T32GM07205 to W. Hancock-Cerutti), from the Michael J. Fox Foundation for Parkinson's Research and the Kavli Foundation (to P. De Camilli), and a National Science Foundation graduate research fellowship (to N. Kumar). Structure determination is based upon research conducted at the Cornell University Northeastern Collaborative Access Team beamlines, which are funded by the National Institute of General Medical Sciences (P41 GM103403). The Pilatus 6M detector on 24-ID-C beam line is funded by a National Institutes of Health–Office of Research Infrastructure Programs High-End Instrumentation grant (S10 RR029205). Data and coordinates for $Vps13_{crystal}$ have been deposited in the Protein Data Bank (accession number 6CBC).

The authors declare no competing financial interests.

Author contributions: N. Kumar designed and performed all the biochemical assays for lipid binding and transfer, purified and crystallized $Vps13_{crystal}$, and determined the structure with F.A. Horenkamp. M. Leonzino coordinated all the cell biology experiments including gene editing as well as designed and performed experiments with VPS13A. W. Hancock-Cerutti designed performed all experiments with VPS13C. J.A. Lees determined the single-particle reconstruction of negative-stained Vps13α. P. Li designed and made the $Vps13_{1–729}$ and $Vps13_{1–1,390}$ fragments for use in the binding experiment in Fig. 5 H and produced protein for the 3D reconstruction. H. Wheeler performed EM analysis. P. De Camilli and K.M. Reinisch designed and supervised the project. The manuscript was prepared by P. De Camilli, K.M. Reinisch, and M. Leonzino with help from W. Hancock-Cerutti and N. Kumar.

Submitted: 3 July 2018
Revised: 13 July 2018
Accepted: 17 July 2018

References

Abeliovich, A., and A.D. Gitler. 2016. Defects in trafficking bridge Parkinson's disease pathology and genetics. *Nature.* 539:207–216. https://doi.org/10.1038/nature20414

Adams, P.D., P.V. Afonine, G. Bunkóczi, V.B. Chen, I.W. Davis, N. Echols, J.J. Headd, L.W. Hung, G.J. Kapral, R.W. Grosse-Kunstleve, et al. 2010. PHENIX: a comprehensive Python-based system for macromolecular structure solution. *Acta Crystallogr. D Biol. Crystallogr.* 66:213–221. https://doi.org/10.1107/S0907444909052925

AhYoung, A.P., J. Jiang, J. Zhang, X. Khoi Dang, J.A. Loo, Z.H. Zhou, and P.F. Egea. 2015. Conserved SMP domains of the ERMES complex bind phospholipids and mediate tether assembly. *Proc. Natl. Acad. Sci. USA.* 112:E3179–E3188. https://doi.org/10.1073/pnas.1422363112

Alesutan, I., J. Seifert, T. Pakladok, J. Rheinlaender, A. Lebedeva, S.T. Towhid, C. Stournaras, J. Voelkl, T.E. Schäffer, and F. Lang. 2013. Chorein sensitivity of actin polymerization, cell shape and mechanical stiffness of vascular endothelial cells. *Cell. Physiol. Biochem.* 32:728–742. https://doi.org/10.1159/000354475

Anding, A.L., C. Wang, T.K. Chang, D.A. Sliter, C.M. Powers, K. Hofmann, R.J. Youle, and E.H. Baehrecke. 2018. Vps13D Encodes a Ubiquitin-Binding Protein that Is Required for the Regulation of Mitochondrial Size and Clearance. *Curr. Biol.* 28:287–295.

Aoun, M., P.A. Corsetto, G. Nugue, G. Montorfano, E. Ciusani, D. Crouzier, P. Hogarth, A. Gregory, S. Hayflick, G. Zorzi, et al. 2017. Changes in Red Blood Cell membrane lipid composition: A new perspective into the pathogenesis of PKAN. *Mol. Genet. Metab.* 121:180–189. https://doi.org/10.1016/j.ymgme.2017.04.006

Bian, X., Y. Saheki, and P. De Camilli. 2018. Ca^{2+} releases E-Syt1 autoinhibition to couple ER-plasma membrane tethering with lipid transport. *EMBO J.* 37:219–234. https://doi.org/10.15252/embj.201797359

Bird, T.D., S. Cederbaum, R.W. Valey, and W.L. Stahl. 1978. Familial degeneration of the basal ganglia with acanthocytosis: a clinical, neuropathological, and neurochemical study. *Ann. Neurol.* 3:253–258. https://doi.org/10.1002/ana.410030312

De, M., A.N. Oleskie, M. Ayyash, S. Dutta, L. Mancour, M.E. Abazeed, E.J. Brace, G. Skiniotis, and R.S. Fuller. 2017. The Vps13p-Cdc31p complex is directly required for TGN late endosome transport and TGN homotypic fusion. *J. Cell Biol.* 216:425–439. https://doi.org/10.1083/jcb.201606078

Dimmer, K.S., and D. Rapaport. 2017. Mitochondrial contact sites as platforms for phospholipid exchange. *Biochim. Biophys. Acta.* 1862:69–80. https://doi.org/10.1016/j.bbalip.2016.07.010

Dong, R., Y. Saheki, S. Swarup, L. Lucast, J.W. Harper, and P. De Camilli. 2016. Endosome-ER Contacts Control Actin Nucleation and Retromer Function through VAP-Dependent Regulation of PI4P. *Cell.* 166:408–423. https://doi.org/10.1016/j.cell.2016.06.037

Doublié, S. 1997. [29] Preparation of selenomethionyl proteins for phase determination. *Methods Enzymol.* 276:523–530. https://doi.org/10.1016/S0076-6879(97)76075-0

Drin, G., J.F. Casella, R. Gautier, T. Boehmer, T.U. Schwartz, and B. Antonny. 2007. A general amphipathic alpha-helical motif for sensing membrane curvature. *Nat. Struct. Mol. Biol.* 14:138–146. https://doi.org/10.1038/nsmb1194

Elbaz-Alon, Y., E. Rosenfeld-Gur, V. Shinder, A.H. Futerman, T. Geiger, and M. Schuldiner. 2014. A dynamic interface between vacuoles and mitochondria in yeast. *Dev. Cell.* 30:95–102. https://doi.org/10.1016/j.devcel.2014.06.007

Emsley, P., B. Lohkamp, W.G. Scott, and K. Cowtan. 2010. Features and development of Coot. *Acta Crystallogr. D Biol. Crystallogr.* 66:486–501. https://doi.org/10.1107/S0907444910007493

Evans, P.R. 2011. An introduction to data reduction: space-group determination, scaling and intensity statistics. *Acta Crystallogr. D Biol. Crystallogr.* 67:282–292. https://doi.org/10.1107/S090744491003982X

Fidler, D.R., S.E. Murphy, K. Courtis, P. Antonoudiou, R. El-Tohamy, J. Ient, and T.P. Levine. 2016. Using HHsearch to tackle proteins of unknown function: A pilot study with PH domains. *Traffic.* 17:1214–1226. https://doi.org/10.1111/tra.12432

Föller, M., A. Hermann, S. Gu, I. Alesutan, S.M. Qadri, O. Borst, E.M. Schmidt, F. Schiele, J.M. vom Hagen, C. Saft, et al. 2012. Chorein-sensitive polymerization of cortical actin and suicidal cell death in chorea-acanthocytosis. *FASEB J.* 26:1526–1534. https://doi.org/10.1096/fj.11-198317

Galmes, R., A. Houcine, A.R. van Vliet, P. Agostinis, C.L. Jackson, and F. Giordano. 2016. ORP5/ORP8 localize to endoplasmic reticulum-mitochondria contacts and are involved in mitochondrial function. *EMBO Rep.* 17:800–810. https://doi.org/10.15252/embr.201541108

Gatta, A.T., and T.P. Levine. 2017. Piecing Together the Patchwork of Contact Sites. *Trends Cell Biol.* 27:214–229. https://doi.org/10.1016/j.tcb.2016.08.010

Gauthier, J., I.A. Meijer, D. Lessel, N.E. Mencacci, D. Krainc, M. Hempel, K. Tsiakas, H. Prokisch, E. Rossignol, M.H. Helm, et al. 2018. Recessive mutations in >VPS13D cause childhood onset movement disorders. *Ann. Neurol.* https://doi.org/10.1002/ana.25204

Gautier, R., D. Douguet, B. Antonny, and G. Drin. 2008. HELIQUEST: a web server to screen sequences with specific alpha-helical properties. *Bioinformatics.* 24:2101–2102. https://doi.org/10.1093/bioinformatics/btn392

Grippa, A., L. Buxó, G. Mora, C. Funaya, F.Z. Idrissi, F. Mancuso, R. Gomez, J. Muntanyà, E. Sabidó, and P. Carvalho. 2015. The seipin complex Fld1/Ldb16 stabilizes ER-lipid droplet contact sites. *J. Cell Biol.* 211:829–844. https://doi.org/10.1083/jcb.201502070

Hanekamp, T., M.K. Thorsness, I. Rebbapragada, E.M. Fisher, C. Seebart, M.R. Darland, J.A. Coxbill, D.L. Updike, and P.E. Thorsness. 2002. Maintenance of mitochondrial morphology is linked to maintenance of the mitochondrial genome in Saccharomyces cerevisiae. *Genetics.* 162:1147–1156.

Hang, L., J. Thundyil, and K.L. Lim. 2015. Mitochondrial dysfunction and Parkinson disease: a Parkin-AMPK alliance in neuroprotection. *Ann. N. Y. Acad. Sci.* 1350:37–47. https://doi.org/10.1111/nyas.12820

Hendrickson, W.A. 1991. Determination of macromolecular structures from anomalous diffraction of synchrotron radiation. *Science.* 254:51–58. https://doi.org/10.1126/science.1925561

Hirabayashi, Y., S.K. Kwon, H. Paek, W.M. Pernice, M.A. Paul, J. Lee, P. Erfani, A. Raczkowski, D.S. Petrey, L.A. Pon, and F. Polleux. 2017. ER-mitochondria tethering by PDZD8 regulates Ca^{2+} dynamics in mammalian neurons. *Science.* 358:623–630. https://doi.org/10.1126/science.aan6009

Holmes, S.E., E. O'Hearn, A. Rosenblatt, C. Callahan, H.S. Hwang, R.G. Ingersoll-Ashworth, A. Fleisher, G. Stevanin, A. Brice, N.T. Potter, et al. 2001. A repeat expansion in the gene encoding junctophilin-3 is associated with Huntington disease-like 2. *Nat. Genet.* 29:377–378. https://doi.org/10.1038/ng760

Holthuis, J.C., and A.K. Menon. 2014. Lipid landscapes and pipelines in membrane homeostasis. *Nature.* 510:48–57. https://doi.org/10.1038/nature13474

Honisch, S., S. Gu, J.M. Vom Hagen, S. Alkahtani, A.A. Al Kahtane, A. Tsapara, A. Hermann, A. Storch, L. Schöls, F. Lang, and C. Stournaras. 2015. Chorein Sensitive Arrangement of Cytoskeletal Architecture. *Cell. Physiol. Biochem.* 37:399–408. https://doi.org/10.1159/000430363

Hönscher, C., M. Mari, K. Auffarth, M. Bohnert, J. Griffith, W. Geerts, M. van der Laan, M. Cabrera, F. Reggiori, and C. Ungermann. 2014. Cellular metabolism regulates contact sites between vacuoles and mitochondria. *Dev. Cell.* 30:86–94. https://doi.org/10.1016/j.devcel.2014.06.006

Hsu, T.H., R.H. Chen, Y.H. Cheng, and C.W. Wang. 2017. Lipid droplets are central organelles for meiosis II progression during yeast sporulation. *Mol. Biol. Cell.* 28:440–451. https://doi.org/10.1091/mbc.e16-06-0375

Huang, Y.J., T.B. Acton, and G.T. Montelione. 2014. DisMeta: a meta server for construct design and optimization. *Methods Mol. Biol.* 1091:3–16. https://doi.org/10.1007/978-1-62703-691-7_1

Jeong, H., J. Park, and C. Lee. 2016. Crystal structure of Mdm12 reveals the architecture and dynamic organization of the ERMES complex. *EMBO Rep.* 17:1857–1871. https://doi.org/10.15252/embr.201642706

John Peter, A.T., B. Herrmann, D. Antunes, D. Rapaport, K.S. Dimmer, and B. Kornmann. 2017. Vps13-Mcp1 interact at vacuole-mitochondria interfaces and bypass ER-mitochondria contact sites. *J. Cell Biol.* 216:3219–3229. https://doi.org/10.1083/jcb.201610055

Kabsch, W. 2010. Integration, scaling, space-group assignment and post-refinement. *Acta Crystallogr. D Biol. Crystallogr.* 66:133–144. https://doi.org/10.1107/S0907444909047374

Källberg, M., H. Wang, S. Wang, J. Peng, Z. Wang, H. Lu, and J. Xu. 2012. Template-based protein structure modeling using the RaptorX web server. *Nat. Protoc.* 7:1511–1522. https://doi.org/10.1038/nprot.2012.085

Kelley, L.A., S. Mezulis, C.M. Yates, M.N. Wass, and M.J.E. Sternberg. 2015. The Phyre2 web portal for protein modeling, prediction and analysis. *Nat. Protoc.* 10:845–858. https://doi.org/10.1038/nprot.2015.053

Knorr, R.L., R. Dimova, and R. Lipowsky. 2012. Curvature of double-membrane organelles generated by changes in membrane size and composition. *PLoS One.* 7:e32753. https://doi.org/10.1371/journal.pone.0032753

Kolehmainen, J., G.C. Black, A. Saarinen, K. Chandler, J. Clayton-Smith, A.L. Träskelin, R. Perveen, S. Kivitie-Kallio, R. Norio, M. Warburg, et al. 2003. Cohen syndrome is caused by mutations in a novel gene, COH1, encoding a transmembrane protein with a presumed role in vesicle-mediated sorting and intracellular protein transport. *Am. J. Hum. Genet.* 72:1359–1369. https://doi.org/10.1086/375454

Kornmann, B., E. Currie, S.R. Collins, M. Schuldiner, J. Nunnari, J.S. Weissman, and P. Walter. 2009. An ER-mitochondria tethering complex revealed by a synthetic biology screen. *Science.* 325:477–481. https://doi.org/10.1126/science.1175088

Lahiri, S., A. Toulmay, and W.A. Prinz. 2015. Membrane contact sites, gateways for lipid homeostasis. *Curr. Opin. Cell Biol.* 33:82–87. https://doi.org/10.1016/j.ceb.2014.12.004

Lang, A.B., A.T. John Peter, P. Walter, and B. Kornmann. 2015. ER-mitochondrial junctions can be bypassed by dominant mutations in the endosomal protein Vps13. *J. Cell Biol.* 210:883–890. https://doi.org/10.1083/jcb.201502105

Lees, J.A., M. Messa, E.W. Sun, H. Wheeler, F. Torta, M.R. Wenk, P. De Camilli, and K.M. Reinisch. 2017. Lipid transport by TMEM24 at ER-plasma membrane contacts regulates pulsatile insulin secretion. *Science.* 355:eaah6171. https://doi.org/10.1126/science.aah6171

Lesage, S., V. Drouet, E. Majounie, V. Deramecourt, M. Jacoupy, A. Nicolas, F. Cormier-Dequaire, S.M. Hassoun, C. Pujol, S. Ciura, et al. International Parkinson's Disease Genomics Consortium (IPDGC). 2016. Loss of VPS13C Function in Autosomal-Recessive Parkinsonism Causes Mitochondrial Dysfunction and Increases PINK1/Parkin-Dependent Mitophagy. *Am. J. Hum. Genet.* 98:500–513. https://doi.org/10.1016/j.ajhg.2016.01.014

Lupo, F., E. Tibaldi, A. Matte, A.K. Sharma, A.M. Brunati, S.L. Alper, C. Zancanaro, D. Benati, A. Siciliano, M. Bertoldi, et al. 2016. A new molecular link between defective autophagy and erythroid abnormalities in chorea-acanthocytosis. *Blood.* 128:2976–2987. https://doi.org/10.1182/blood-2016-07-727321

McCray, B.A., E. Skordalakes, and J.P. Taylor. 2010. Disease mutations in Rab7 result in unregulated nucleotide exchange and inappropriate activation. *Hum. Mol. Genet.* 19:1033–1047. https://doi.org/10.1093/hmg/ddp567

Muñoz-Braceras, S., R. Calvo, and R. Escalante. 2015. TipC and the chorea-acanthocytosis protein VPS13A regulate autophagy in Dictyostelium and human HeLa cells. *Autophagy.* 11:918–927. https://doi.org/10.1080/15548627.2015.1034413

Murphy, S.E., and T.P. Levine. 2016. VAP, a Versatile Access Point for the Endoplasmic Reticulum: Review and analysis of FFAT-like motifs in the VAPome. *Biochim. Biophys. Acta.* 1861(8, 8 Pt B):952–961. https://doi.org/10.1016/j.bbalip.2016.02.009

Park, J.S., and A.M. Neiman. 2012. VPS13 regulates membrane morphogenesis during sporulation in Saccharomyces cerevisiae. *J. Cell Sci.* 125:3004–3011. https://doi.org/10.1242/jcs.105114

Park, J.S., Y. Okumura, H. Tachikawa, and A.M. Neiman. 2013. SPO71 encodes a developmental stage-specific partner for Vps13 in Saccharomyces cerevisiae. *Eukaryot. Cell.* 12:1530–1537. https://doi.org/10.1128/EC.00239-13

Park, J.S., M.K. Thorsness, R. Policastro, L.L. McGoldrick, N.M. Hollingsworth, P.E. Thorsness, and A.M. Neiman. 2016. Yeast Vps13 promotes mitochondrial function and is localized at membrane contact sites. *Mol. Biol. Cell.* 27:2435–2449. https://doi.org/10.1091/mbc.e16-02-0112

Pelzl, L., B. Elsir, I. Sahu, R. Bissinger, Y. Singh, B. Sukkar, S. Honisch, L. Schoels, M. Jemaà, E. Lang, et al. 2017. Lithium Sensitivity of Store Operated Ca2+ Entry and Survival of Fibroblasts Isolated from Chorea-Acanthocytosis Patients. *Cell. Physiol. Biochem.* 42:2066–2077. https://doi.org/10.1159/000479901

Pfisterer, S.G., D. Bakula, T. Frickey, A. Cezanne, D. Brigger, M.P. Tschan, H. Robenek, and T. Proikas-Cezanne. 2014. Lipid droplet and early autophagosomal membrane targeting of Atg2A and Atg14L in human tumor cells. *J. Lipid Res.* 55:1267–1278. https://doi.org/10.1194/jlr.M046359

Rampoldi, L., C. Dobson-Stone, J.P. Rubio, A. Danek, R.M. Chalmers, N.W. Wood, C. Verellen, X. Ferrer, A. Malandrini, G.M. Fabrizi, et al. 2001. A conserved sorting-associated protein is mutant in chorea-acanthocytosis. *Nat. Genet.* 28:119–120. https://doi.org/10.1038/88821

Ramseyer, V.D., V.A. Kimler, and J.G. Granneman. 2018. Vacuolar protein sorting 13C is a novel lipid droplet protein that inhibits lipolysis in brown adipocytes. *Mol. Metab.* 7:57–70. https://doi.org/10.1016/j.molmet.2017.10.014

Richardson, C.D., G.J. Ray, M.A. DeWitt, G.L. Curie, and J.E. Corn. 2016. Enhancing homology-directed genome editing by catalytically active and inactive CRISPR-Cas9 using asymmetric donor DNA. *Nat. Biotechnol.* 34:339–344. https://doi.org/10.1038/nbt.3481

Rowe, E.R., M.L. Mimmack, A.D. Barbosa, A. Haider, I. Isaac, M.M. Ouberai, A.R. Thiam, S. Patel, V. Saudek, S. Siniossoglou, and D.B. Savage. 2016. Conserved Amphipathic Helices Mediate Lipid Droplet Targeting of Perilipins 1-3. *J. Biol. Chem.* 291:6664–6678. https://doi.org/10.1074/jbc.M115.691048

Saheki, Y., and P. De Camilli. 2017. Endoplasmic Reticulum-Plasma Membrane Contact Sites. *Annu. Rev. Biochem.* 86:659–684. https://doi.org/10.1146/annurev-biochem-061516-044932

Saheki, Y., X. Bian, C.M. Schauder, Y. Sawaki, M.A. Surma, C. Klose, F. Pincet, K.M. Reinisch, and P. De Camilli. 2016. Control of plasma membrane lipid homeostasis by the extended synaptotagmins. *Nat. Cell Biol.* 18:504–515. https://doi.org/10.1038/ncb3339

Samaranayake, H.S., A.E. Cowan, and L.A. Klobutcher. 2011. Vacuolar protein sorting protein 13A, TtVPS13A, localizes to the tetrahymena thermophila phagosome membrane and is required for efficient phagocytosis. *Eukaryot. Cell.* 10:1207–1218. https://doi.org/10.1128/EC.05089-11

Schauder, C.M., X. Wu, Y. Saheki, P. Narayanaswamy, F. Torta, M.R. Wenk, P. De Camilli, and K.M. Reinisch. 2014. Structure of a lipid-bound extended synaptotagmin indicates a role in lipid transfer. *Nature.* 510:552–555. https://doi.org/10.1038/nature13269

Schmidt, E.M., E. Schmid, P. Münzer, A. Hermann, A.K. Eyrich, A. Russo, B. Walker, S. Gu, J.M. vom Hagen, C. Faggio, et al. 2013. Chorein sensitivity of cytoskeletal organization and degranulation of platelets. *FASEB J.* 27:2799–2806. https://doi.org/10.1096/fj.13-229286

Seifert, W., J. Kühnisch, T. Maritzen, D. Horn, V. Haucke, and H.C. Hennies. 2011. Cohen syndrome-associated protein, COH1, is a novel, giant Golgi matrix protein required for Golgi integrity. *J. Biol. Chem.* 286:37665–37675. https://doi.org/10.1074/jbc.M111.267971

Seifert, W., J. Kühnisch, T. Maritzen, S. Lommatzsch, H.C. Hennies, S. Bachmann, D. Horn, and V. Haucke. 2015. Cohen syndrome-associated protein COH1 physically and functionally interacts with the small GTPase RAB6 at the Golgi complex and directs neurite outgrowth. *J. Biol. Chem.* 290:3349–3358. https://doi.org/10.1074/jbc.M114.608174

Seong, E., R. Insolera, M. Dulovic, E.J. Kamsteeg, J. Trinh, N. Brüggemann, E. Sandford, S. Li, A.B. Ozel, J.Z. Li, et al. 2018. Mutations in VPS13D lead to a new recessive ataxia with spasticity and mitochondrial defects. *Ann. Neurol.* https://doi.org/10.1002/ana.25220

Sherman, D.J., R. Xie, R.J. Taylor, A.H. George, S. Okuda, P.J. Foster, D.J. Needleman, and D. Kahne. 2018. Lipopolysaccharide is transported to the cell surface by a membrane-to-membrane protein bridge. *Science.* 359:798–801. https://doi.org/10.1126/science.aar1886

Shi, L., K. Howan, Q.T. Shen, Y.J. Wang, J.E. Rothman, and F. Pincet. 2013. Preparation and characterization of SNARE-containing nanodiscs and direct study of cargo release through fusion pores. *Nat. Protoc.* 8:935–948. https://doi.org/10.1038/nprot.2013.048

Shiokawa, N., M. Nakamura, M. Sameshima, A. Deguchi, T. Hayashi, N. Sasaki, and A. Sano. 2013. Chorein, the protein responsible for chorea-acanthocytosis, interacts with β-adducin and β-actin. *Biochem. Biophys. Res. Commun.* 441:96–101. https://doi.org/10.1016/j.bbrc.2013.10.011

Struck, D.K., D. Hoekstra, and R.E. Pagano. 1981. Use of resonance energy transfer to monitor membrane fusion. *Biochemistry.* 20:4093–4099. https://doi.org/10.1021/bi00517a023

Tamura, N., T. Nishimura, Y. Sakamaki, I. Koyama-Honda, H. Yamamoto, and N. Mizushima. 2017. Differential requirement for ATG2A domains for localization to autophagic membranes and lipid droplets. *FEBS Lett.* 591:3819–3830. https://doi.org/10.1002/1873-3468.12901

Ueno, S., Y. Maruki, M. Nakamura, Y. Tomemori, K. Kamae, H. Tanabe, Y. Yamashita, S. Matsuda, S. Kaneko, and A. Sano. 2001. The gene encoding a newly discovered protein, chorein, is mutated in chorea-acanthocytosis. *Nat. Genet.* 28:121–122. https://doi.org/10.1038/88825

Velayos-Baeza, A., A. Vettori, R.R. Copley, C. Dobson-Stone, and A.P. Monaco. 2004. Analysis of the human VPS13 gene family. *Genomics.* 84:536–549. https://doi.org/10.1016/j.ygeno.2004.04.012

Velikkakath, A.K., T. Nishimura, E. Oita, N. Ishihara, and N. Mizushima. 2012. Mammalian Atg2 proteins are essential for autophagosome formation and important for regulation of size and distribution of lipid droplets. *Mol. Biol. Cell.* 23:896–909. https://doi.org/10.1091/mbc.e11-09-0785

Voelker, D.R. 1984. Phosphatidylserine functions as the major precursor of phosphatidylethanolamine in cultured BHK-21 cells. *Proc. Natl. Acad. Sci. USA.* 81:2669–2673. https://doi.org/10.1073/pnas.81.9.2669

Vonk, J.J., W.M. Yeshaw, F. Pinto, A.I.E. Faber, L.L. Lahaye, B. Kanon, M. van der Zwaag, A. Velayos-Baeza, R. Freire, S.C. van IJzendoorn, et al. 2017. Drosophila Vps13 Is Required for Protein Homeostasis in the Brain. *PLoS One.* 12:e0170106. https://doi.org/10.1371/journal.pone.0170106

Walsh, M.T., E. Di Leo, I. Okur, P. Tarugi, and M.M. Hussain. 2016. Structure-function analyses of microsomal triglyceride transfer protein missense mutations in abetalipoproteinemia and hypobetalipoproteinemia subjects. *Biochim. Biophys. Acta.* 1861:1623–1633. https://doi.org/10.1016/j.bbalip.2016.07.015

Wang, C.W., J. Kim, W.P. Huang, H. Abeliovich, P.E. Stromhaug, W.A. Dunn Jr., and D.J. Klionsky. 2001. Apg2 is a novel protein required for the cytoplasm to vacuole targeting, autophagy, and pexophagy pathways. *J. Biol. Chem.* 276:30442–30451. https://doi.org/10.1074/jbc.M102342200

Weber, T., B.V. Zemelman, J.A. McNew, B. Westermann, M. Gmachl, F. Parlati, T.H. Söllner, and J.E. Rothman. 1998. SNAREpins: minimal machinery for membrane fusion. *Cell.* 92:759–772. https://doi.org/10.1016/S0092-8674(00)81404-X

Wong, L.H., A. Čopič, and T.P. Levine. 2017. Advances on the Transfer of Lipids by Lipid Transfer Proteins. *Trends Biochem. Sci.* 42:516–530. https://doi.org/10.1016/j.tibs.2017.05.001

Yang, R.Y., H. Xue, L. Yu, A. Velayos-Baeza, A.P. Monaco, and F.T. Liu. 2016. Identification of VPS13C as a Galectin-12-Binding Protein That Regulates Galectin-12 Protein Stability and Adipogenesis. *PLoS One.* 11:e0153534. https://doi.org/10.1371/journal.pone.0153534

Yu, H., Y. Liu, D.R. Gulbranson, A. Paine, S.S. Rathore, and J. Shen. 2016. Extended synaptotagmins are Ca2+-dependent lipid transfer proteins at membrane contact sites. *Proc. Natl. Acad. Sci. USA.* 113:4362–4367. https://doi.org/10.1073/pnas.1517259113